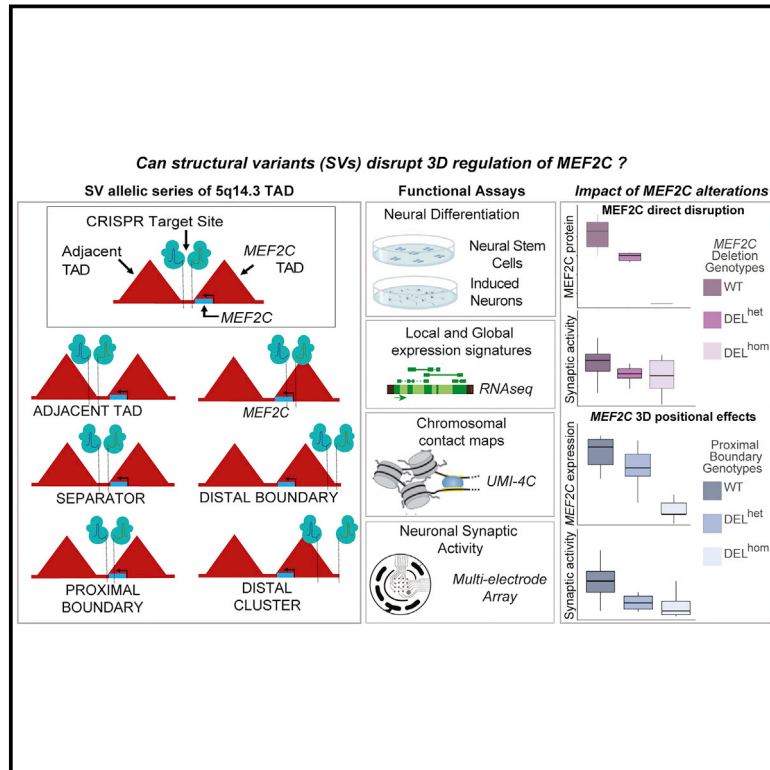# Transcriptional and functional consequences of alterations to *MEF2C* and its topological organization in neuronal models

Graphical abstract

Authors

Kiana Mohajeri, Rachita Yadav,
Eva D'haene, ..., James F. Gusella,
Sarah Vergult, Michael E. Talkowski

Correspondence

mtalkowski@mgh.harvard.edu

The authors present functional characterization of a CRISPR-engineered allelic series of deletions altering *MEF2C* and the 3D regulatory architecture encompassing the 5q14.3 microdeletion syndrome region. They find that direct deletion of *MEF2C* and some, but not all, 3D regulatory interactions result in shared transcriptional and electrophysiological deficits in early neurodevelopment.

CellPress

Transcriptional and functional consequences of alterations to *MEF2C* and its topological organization in neuronal models

Kiana Mohajeri,[1,2,3,4,5,15] Rachita Yadav,[1,2,3,4,15] Eva D'haene,[6] Philip M. Boone,[1,2,3,7] Serkan Erdin,[1,2,3] Dadi Gao,[1,2,3,4] Mariana Moyses-Oliveira,[1,2,3,4] Riya Bhavsar,[1,2,3] Benjamin B. Currall,[1,2,3] Kathryn O'Keefe,[1,2,3] Nicholas D. Burt,[1,2,3] Chelsea Lowther,[1,2,3,4] Diane Lucente,[1,4] Monica Salani,[1,2,3] Mathew Larson,[1] Claire Redin,[1,14] Olga Dudchenko,[8,9] Erez Lieberman Aiden,[8,9,10,11,12] Björn Menten,[6] Derek J.C. Tai,[1,2,3,4] James F. Gusella,[1,3,5,13] Sarah Vergult,[6] and Michael E. Talkowski[1,2,3,4,5,*]

Summary

Point mutations and structural variants that directly disrupt the coding sequence of *MEF2C* have been associated with a spectrum of neurodevelopmental disorders (NDDs). However, the impact of *MEF2C* haploinsufficiency on neurodevelopmental pathways and synaptic processes is not well understood, nor are the complex mechanisms that govern its regulation. To explore the functional changes associated with structural variants that alter *MEF2C* expression and/or regulation, we generated an allelic series of 204 isogenic human induced pluripotent stem cell (hiPSC)-derived neural stem cells and glutamatergic induced neurons. These neuronal models harbored CRISPR-engineered mutations that involved direct deletion of *MEF2C* or deletion of the boundary points for topologically associating domains (TADs) and chromatin loops encompassing *MEF2C*. Systematic profiling of mutation-specific alterations, contrasted to unedited controls that were exposed to the same guide RNAs for each edit, revealed that deletion of *MEF2C* caused differential expression of genes associated with neurodevelopmental pathways and synaptic function. We also discovered significant reduction in synaptic activity measured by multielectrode arrays (MEAs) in neuronal cells. By contrast, we observed robust buffering against *MEF2C* regulatory disruption following deletion of a distal 5q14.3 TAD and loop boundary, whereas homozygous loss of a proximal loop boundary resulted in down-regulation of *MEF2C* expression and reduced electrophysiological activity on MEA that was comparable to direct gene disruption. Collectively, these studies highlight the considerable functional impact of *MEF2C* deletion in neuronal cells and systematically characterize the complex interactions that challenge *a priori* predictions of regulatory consequences from structural variants that disrupt three-dimensional genome organization.

Introduction

Over the last decade, genetic studies have established haploinsufficiency of *MEF2C* (MIM: 600662) as a cause of neurodevelopmental disorders (NDDs).[1] Microarray and sequencing studies have repeatedly implicated loss-of-function (LoF) mutations in *MEF2C* etiological factors across numerous syndromic and isolated NDD phenotypes.[2–7] To date, these mutational mechanisms have included protein-truncating variants (PTVs), structural variants (SVs) involving deletions and balanced chromosomal abnormalities (BCAs), and broader microdeletion of the 5q14.3 locus.[2,8–10] Mouse models with conditionally modulated *Mef2c* expression[1,3–5,11,12] in neural tissue also display fundamentally altered brain development and neuronal activity.[13–17] The extensive complementary data from human affected individuals and mouse models suggests that *MEF2C* LoF mutations underlie aberrant neurodevelopment with varied consequences that include developmental delay, intellectual disability, autism spectrum disorder (ASD), hypotonia, and epilepsy.[1,6,11,18–22] To date, the mechanisms associated with haploinsufficiency of *MEF2C* that contribute to these phenotypic presentations have not been explored in human neuronal models, which can provide insights into signatures of *MEF2C*-specific changes as well as evidence of transcriptional or functional convergence across NDDs.

In contrast to the abundant molecular studies of direct gene disruption in NDDs, functional interpretation of noncoding variation remains a considerable challenge.[23,24] Multiple recent studies have described highly penetrant noncoding mutations across rare NDDs

and Mendelian disorders,[25–27] and one emerging mutational mechanism not captured by exome and genome sequencing is regulatory changes associated with three-dimensional (3D) genome reorganization.[28–30] Early glimpses into the intricacies of 3D genome architecture demonstrated the partitioning of chromatin into topologically associating domains (TADs) and the smaller loops within them. It is presently understood that TADs demarcate neighborhoods of long-range regulatory interaction, while loops facilitate punctate enhancer and promoter connections.[31,32] Some prior studies have discovered pathogenic consequences from positional effects through the disruption of TADs and loops,[31,33–35] while others suggest an uncoupling of topological rewiring and gene expression.[29,32,36,37] These studies collectively underscore the complexity of long-range regulatory mechanisms and suggest that functional alterations associated with structural variants of 3D organization are likely to be context specific and require extensive experimental modeling to dissect the diverse regulatory mechanisms of individual loci.

We previously demonstrated through whole-genome sequencing of NDD cases that chromosome 5q14.3 harbored an unusual and genome-wide significant excess of noncoding BCA breakpoints that did not directly disrupt *MEF2C* but that all occurred within the TAD boundaries encompassing *MEF2C*.[38] This distribution of breakpoints in proximity to *MEF2C* was further supported by microdeletions in NDD cases reported in DECIPHER that apparently did not directly alter the locus (at the available resolution of chromosomal microarray).[39] In considering the landscape of *de novo* SVs across the 5q14.3 locus in NDD cases, the unifying thread appears to be recurrent distal boundary disruption. Taken together, these data suggest that direct disruption of *MEF2C* and alterations to its 3D regulatory architecture may result in comparable molecular mechanisms in NDD cases. Motivated by these findings, we performed a systematic molecular dissection of the 5q14.3 locus to quantify the transcriptomic and electrophysiological effects of *MEF2C* LoF in human neural derivatives. Through the generation of an allelic series of CRISPR-engineered human induced pluripotent stem cell (hiPSC)-derived neural stem cells (NSCs) and glutamatergic induced neurons (iNs), we interrogated the impact of enhancer, TAD boundary, and loop boundary deletion on local genome organization, local expression effects on *MEF2C*, and global transcriptional signatures. Our analyses revealed that direct *MEF2C* alteration results in both transcriptional and functional changes to the synapse. These studies further revealed that disruption of the distal boundary of the *MEF2C*-containing loop was insufficient to produce indirect dysregulation of *MEF2C* expression, whereas disruption of the proximal boundary of the same 3D structure resulted in reduced expression of *MEF2C* with functional consequences that were comparable to direct gene deletion. Overall, these data suggest that the effects of direct and indirect disruption of

MEF2C contributes to cell-type-specific alterations on neuronal functions that converge on synaptic deficits in neurodevelopment.

Material and methods

hiPSC culture

All studies involved secondary use of publicly available cell lines and/or data and were approved by the Institutional Review Board of Mass General Brigham. The GM08330 hiPSCs were grown in feeder-free culture via Matrigel with Essential 8 media. Cells were passaged with ReLeS. mFreSR was used for cryopreservation. Y-27632 dihydrochloride was added to media at 1 mg/mL for up to 24 h for initial plating and at various points in the engineering protocol as indicated below.

In silico CRISPR guide selection

Dual guides were designed with multiple considerations to maximize on-target cutting efficiency for deletion generation while minimizing both off-target effects. Guides with NGG PAM for Cas9 were identified with the MIT CRISPR design tool.[40] Off-target characterization was conducted per guide with Off-Spotter.[41] We restricted to guides without identified coding, long noncoding RNAs (lncRNAs), ribosomal RNA (rRNA), or transfer RNA (tRNA) off-target hits with ≤4 mismatches between the guide and the off-target position (Table S1).

CRISPR-Cas9 transfection

To generate CRISPR-edited lines, hiPSCs were transiently transfected with breakpoint targeting guides and SpCas9 ribonuclear protein as ribonuclear proteins (RNP). Alt-R SpCas9 Nuclease was diluted to 25 μM in 20 mM HEPES Buffer and 150 mM KCl. We diluted custom designed Alt-R CRISPR RNAs (crRNAs; IDT) and Alt-R *trans*-activating CRISPR RNA (tracrRNA; IDT, 1072532) to 25 μM and annealed them by using manufacturer recommendations to create crRNA::tracrRNA duplexes. We generated single-cell hiPSC suspension of Y-27632 dihydrochloride-treated cells by using and filtering them through a 40 μM mesh (1 μg), and we combined annealed guides (37.5 μM total) with 1 μg pmaxGFP plasmid and nucleofected them into hiPSCs (5×10^5 cells per transfection). Nucleofections were conducted with an Amaxa Nucleofector II, program A-033, with Human Stem Cell Nucleofector Kit 1 following manufacturer's instructions. Nucleofected cells were plated onto Matrigel-coated 12-well plates and maintained in E8 media supplemented with Y-27632 dihydrochloride at 1 mg/mL for 24 h. Cell-containing wells were replenished with E8 media daily with subsequent fluorescence-activated cell sorting (FACS) 36–48 h after transfection. The transfected cells were FACS sorted and consolidated for clonal isolates.

Genotyping was conducted with custom designed PCR primers (IDT) with Taq polymerase. PCR products were run on 2% Agarose 96-well E-Gels for visualization. Positive products were cleaned up with ExoSAP-IT and submitted for Sanger sequencing (Table S2). As an orthogonal method of genotyping and for confirmation of clonality, edited lines and a subset of wild-type lines identified by Sanger were also genotyped with droplet digital PCR (ddPCR) with DNA copy number probes. When possible, we required six independent clonal lines per genotype at each target locus in the interest of maximizing the number of biological replicates in each experiment. We were unable to generate homozygous deletions

for some target regions, and in some instances when CRISPR editing did not yield the desired number of independent clonal replicates, we split single lines in two to differentiate six lines per genotype and capture technical variation attributable to differentiation as outlined in Table S7.

Selection of TRA-1-60-positive hiPSC CRISPR lines

3–5 passages following FACS, hiPSC lines selected for differentiation underwent magnetic-activated cell sorting (MACS) for expression of the TRA-1-60 cell surface marker to select pluripotent cells for differentiation. Cells were separated with MiniMACS Separator with Anti-TRA-1-60 microbeads following manufacturer instructions ($\sim 2 \times 10^6$ cells per line). TRA-1-60-positive cells were plated with Y-27632 dihydrochloride (1 mg/mL), expanded, and cryopreserved with mFreSR. Cells within three passages of TRA-1-60 selection were used for differentiation.

Differentiation of hiPSCs into iNs

All cell preparations for lentiviral transduction and subsequent iN differentiation were conducted in parallel in a single batch for all lines representing a given locus. To minimize technical artifacts, TRA-1-60 positive hiPSCs were plated as single cells at 80% confluence on a Matrigel-coated 6-well plate with Y-27632 dihydrochloride (1 mg/mL). Polybrene was added at 8 mg/mL 1 h after re-plating. Cells were incubated with polybrene for 10–15 min prior to the addition of lentivirus. Lentiviral constructs for directed differentiation of hiPSCs into iNs were made as described previously.[42]

Differentiation of hiPSCs into neural stem cells

We conducted all preparations for NSC differentiation with all lines for a given locus in the same batch to minimize technical artifacts. 12–18 lines per batch were differentiated, depending on the locus. TRA-1-60-positive lines were differentiated into NSCs with the protocol detailed by Thermo Fisher (MAN0008031). For all target regions, passage 7 (P7) stage NSCs were harvested for RNA extraction, conformation capture crosslinking, or fixation for staining, as described below.

RNA extraction

iNs were harvested on day 24 of differentiation, 5×10^5 cells per 1 mL TRIzol Reagent. NSCs were harvested at the completion of differentiation at P7. Media was aspirated completely from cells with subsequent direct addition of TRIzol Reagent. We had TRIzol-extracted RNA from iNs undergo subsequent RNeasy cleanup with on-column digest to ensure removal of residual DNA that we often observe carrying over in phenol-chloroform-extracted RNA from this cell type. RNA concentration and quality was assessed by TapeStation with RNA integrity number (RIN) ≥ 8 required for downstream use for RNA sequencing (RNA-seq) or qPCR.

RNA-seq library preparation

RNA-seq libraries were prepared by the Genomic and Technology Core (GTC) of Massachusetts General Hospital (MGH) with TruSeq Stranded mRNA Library Kit and prepared according to manufacturer's instructions. In brief, RNA sample quality (based on RIN) and quantity was determined on the basis of TapeStation, and between 100 and 500 ng of total RNA was used to prepare libraries. PolyA bead capture was used to enrich for mRNA, followed by stranded reverse transcription and chemical shearing to make appropriate stranded cDNA inserts for library construction. Libraries are finished by adding sample-specific, dual-barcoded adapters for Illumina sequencing followed by 15 rounds of PCR amplification. Final concentration and size distribution of libraries were evaluated by TapeStation and qPCR with Library Quantification Kit. Libraries were sequenced on an Illumina NovaSeq to an average depth of 30 M paired-end (PE, 60 M total) 150 base-pair (bp) reads.

RNA-seq data processing

We used FastQC to determine the data quality of the sequencing data. The read pairs were then aligned to the human reference genome (GRCh37, Ensembl release 75, v = 47) by STAR 2.5.3[43] with the following parameters "–outFilterMultimapNmax 1 –outFilterMismatchNoverLmax 0.1 –alignEndsType local." We also used STAR aligner to quantify gene-level read counts on the basis of gene annotations inhuman reference genome (GRCh37, Ensembl release 75). Picard (http://broadinstitute.github.io/picard/) and RNAseqQC[44] were used for quality control of the data. Samples with less than 20 M estimated library size as annotated by Picard were removed. We tested a set of neuronal marker genes to confirm the cellular stage of the cell cultures. Samples with failed quality control (QC) were removed from subsequent analyses. Genes with 0.5 counts per million (CPM) cut-off in 50% of samples in at least one condition in a particular comparison were analyzed in differential expression and correlation analyses.

Differential gene expression

Differential expression (DE) analysis was performed with R package DESeq2 version 1.16.1.[45] DE was performed within each cell and edit type and edited samples (heterozygous [DEL^{het}] and homozygous [DEL^{hom}]) were compared to corresponding wild-type (WT) samples. To account for unknown sources of variation in the expression data, surrogate variables (SVs) were estimated with surrogate variable analysis (SVAseq)[46] package with $\sim$ genotype as full model and $\sim$1 as reduced model. We incorporated the estimated SVs into the DESeq2 model as $\sim$ genotype + SVs to identify differentially expressed genes (DEGs) on the basis of the Wald test and corrected p values for multiple testing by using Benjamini-Hochberg-adjusted p values (false discovery rate; FDR). The significant DEGs were identified at FDR < 0.1.

Co-expression analysis

We performed co-expression network analysis by using R package weighted gene co-expression network analysis (WGCNA)[47] for each cell type separately with the signed network type for which we used log-transformed CPM-filtered and SVA-corrected counts. Soft power was selected such that the scale-free topology fit $R^2 > 0.8$. and the smallest module size was set to 50. Merge of the modules with similar eigengene profiles was performed (similarity > 70%). Module membership for each gene was re-evaluated on the basis of the module membership p value; genes with p value > 0.01 were marked as unassigned (module 0).

Functional enrichment analysis

We tested enrichments of DEGs and co-expression module genes by using one-tailed Fisher's exact test for the curated lists of Gene Ontology terms, canonical pathways, Human Phenotype Ontology terms, and transcription factor targets from mSigDB (v7.4)[48,49] and phenotype-informed literature data including gene sets and modules previously published with functional

associations with neurological phenotype, synaptic activity, and *MEF2C* function. These gene sets are mouse model RNA-seq DEG validation;[50] Synaptic genes: Syngo v1.1;[51] *MEF2C* targets: ENCODE LCLs ChIP-seq;[52] DNA-binding and transcription modules;[53] synaptic activity modules;[53] and neuroepithelial precursor and neuron expression modules.[54] The resulting p values were corrected for multiple tests with Benjamini-Hochberg correction. The protein-protein interactions (PPIs) network was generated and annotated for functional association with stringApp[55] in Cytoscape.

ATAC-seq sample and library preparation from WT iNs and NSCs

ATAC-seq was applied to WT NSC clones (n = 6) and WT iN clones (n = 6), and cell lines were independently differentiated for each cell type as described above. ATAC-seq was performed as previously described with minor modifications (details in supplemental methods).[56] The size-selected libraries were run on the Agilent TapeStation tape to determine fragment size profile. Libraries were multiplexed, pooled, and sequenced on an Illumina NovaSeq, generating an average depth of 100 M PE 150 bp reads.

ATAC-seq peak calling from WT NSCs and iNs

ATAC-seq peak calling followed ENCODE guidance.[52] The paired-end reads were aligned to the human reference genome GRCh38 with Bowtie2 version 2.3.1,[57] allowing up to four multiple maps. Alignments were first de-duplicated and the coordinates were adjusted according to TN5 transposase cut. Pseudo-replicates are pooled replicates were generated. Narrow peaks were called by MACS2 version 2.2.7.1,[58] with shift size of 75, smooth window size of 150, and p value < 0.01. Only the top 300,000 peaks were kept for the downstream analyses. We then used the IDR package[59] to cross validate samples and generate conservative and optimal peaks. The genomic coordinates of peak regions were then transferred to the coordinates against GRCh37 with the UCSC tool LiftOver.[60] It is worth noting that all peak regions were successfully transferred to GRCh37 with the same peak length.

Multi-electrode array analysis

48-well multi-electrode array (MEA) plates (Axion Biosystems) were prepared by coating wells with 50 μL 0.1% polyethylenimine (PEI) dissolved in Borate Buffer and sterile filtered with a 0.2 μm filter prior to use. Coated wells were incubated at 37°C for 1 h, followed by a wash to remove PEI and left on room temperature (RT) overnight to dry out. To prepare iNs for electrophysiology readings, we largely followed manufacturer protocol with a few modifications. Briefly, TRA1+ hiPSC lines underwent one post-thaw passage prior to further manipulation. All hiPSC lines for MEA underwent Ngn2 transduction as a single batch to eliminate viral transduction batch effect with the same transduction and selection steps described in "differentiation of hiPSCs into iNs" above. The neurons (27–60 days) continued to undergo half media change every 3 days, but media was changed to BrainPhys to promote spiking activity on the basis of the manufacturer protocol (Axion Biosystems protocol: Culturing Human hiPSC-derived Excitatory Neurons on Microelectrode Arrays: Maestro Pro MEA). MEA plate readings were conducted every 3 days, 18–24 h following each media change. Readings were conducted at 37°C with 0% CO_2 for 15 min with an Axion Biosystems Maestro Pro. Manufacturer-set thresholds for spike and network burst calling were used.

UMI-4C sample preparation, library preparation, and sequencing

We performed UMI-4C according to the protocol by Schwartzman et al.[61] In brief, cells were detached with Accutase, neutralized with PBS and pelleted, resuspended in a PBS/10% FBS solution, and crosslinked using formaldehyde. After centrifugation, pellets were washed, snap-frozen in liquid nitrogen, and stored at −80°C until further processing.

Frozen pellets were resuspended in a 500 μL pre-diluted DpnII buffer, 15 μL pre-heated 10% SDS and incubated on a thermomixer for 1 h at 37°C, shaking at 900 RPM. After adding 150 μL 10% Triton X-100, the solution was incubated again (1 h, 37°C, 900 RPM). We digested the chromatin by using 600 U in three stages (200 U for 2 h, 200 U overnight, 200 U for 2 h) at 37°C and 900 RPM. We incubated the solution at 65°C for 20 min to inactivate the restriction enzyme and put it on ice. Next, we ligated the chromatin by adding 4,000 U of T4 DNA and 10× T4 DNA ligase buffer to a total volume of 1,300 μL and incubating the solution overnight at 16°C and 300 RPM. Ligated chromatin was de-crosslinked by incubation with 8 μL proteinase K (20 mg/mL) (overnight, 65°C, 300 RPM). A 3C template was then purified with 1× Ampure XP beads. Up to 4 μg 3C template per sample was sheared with Covaris to an average fragment length of 300 bp. UMI-4C sequencing libraries were generated with the NEBNext Ultra II library prep kit. For each sample, library included a size selection targeting fragments with a length of 300–400 bp and 4–8 cycles of PCR enrichment. Next, we performed two nested PCR reactions to enrich for fragments captured by the viewpoint of interest, both by using 2 μL 10 mM Illumina enrichment primer 2 and either a viewpoint-specific "upstream" (reaction 1, 2 μL 10 mM) or "downstream" (reaction 2, 2 μL 10 mM) primer. For each sample, we performed up to eight nested PCR reactions in parallel. Between PCR reactions, the product was cleaned up with 1× AmpureXP beads and eluted in 21 μL. The final PCR product was cleaned up with 0.7× AmpureXP beads and eluted in 25 μL. Reactions per sample were pooled and library concentration was quantified via qPCR with the KAPA SYBR FAST qPCR Master Mix. UMI-4C libraries were pooled and sequenced on an Illumina HiSeq or NovaSeq (paired-end, 2 × 150 cycles).

UMI-4C data processing—Delta map generation

Reads were mapped to the GRCh37 human reference genome and filtered on the basis of the presence of the downstream primer sequence (20% mismatch allowed). We used two primer sequences/viewpoints within the *MEF2C* promoter to capture the phasing SNP (details in supplemental methods). We split the sequenced fastq files on the basis of the presence of this SNP and analyzed them separately, and we used them as input to the UMI-4C R package[62] to generate genomic interaction tracks representing UMI counts (i.e., unique interactions) per genomic restriction fragment. We then used the package to generate smoothed, viewpoint-specific interaction profiles for the region of interest. For each profile, interaction counts were normalized to the total UMI count within the profile and the adaptive smoothing parameter (win_cov) was scaled to this statistic as well (with a minimum of 10 and maximum of 180).

UMI-4C data processing—FDR-corrected differential contact annotation

Differential contacts were investigated within chr5: 86,750,000–90,25,0000. A sliding window with size of 5,000 bp and step of

200 bp were applied to this region, which quantified the 4C signals in the sub-regions from each contact track. Generalized linear regression was fit under a negative binomial (NB) distribution with DESeq2 v1.24.0,[45] and Wald test was applied to examine whether there was a significant difference between WT samples and each type of CRISPR samples. The subregions with FDR < 0.1 were considered as significantly differential contacts (details in supplemental methods).

Results

Haploinsufficiency of *MEF2C* is associated with altered expression of highly constrained genes in NSCs and synaptic genes in iNs

There is strong evidence for association between microdeletions and LoF point mutations that disrupt *MEF2C* and a spectrum of NDDs. We therefore first sought to determine the transcriptional changes in early neuronal development stem cells and fully differentiated neurons caused by direct disruption of *MEF2C*. We generated targeted DEL[het] and DEL[hom] deletions of *MEF2C* in hiPSCs by using dual-guide CRISPR-Cas9 genome editing. Following single-cell isolation and screening, we retained both edited clones and matched controls, clones that were exposed to all experimental conditions but did not demonstrate evidence of on-target editing. Six replicates per genotype then underwent differentiation to NSCs and iNs for transcriptional profiling with RNA-seq (Figure 1A). MEF2C protein accumulation was confirmed to be commensurate with zygosity via immunoblot quantification (supplemental methods, section 1; Figures S1–S4).

We performed differential expression analysis by using DESeq2 and SVAseq to account for unknown sources of variation in expression data. In this analysis, differentially expressed genes (DEGs) were selected at Benjamini-Hochberg-corrected p values (FDR) < 0.1. In NSCs, we observed a strong zygosity-dependent transcriptional response to *MEF2C* disruption with 371 and 2,196 DEGs in DEL[het] and DEL[hom], respectively (Figure 1B). By contrast, in iNs we observed 742 DEGs following DEL[het] that were notable for a predominance of upregulated genes and 292 DEGs in DEL[hom] cells. Nonetheless, we found highly significant overlap and directionally concordant DEGs between DEL[het] and DEL[hom] genotypes in both NSCs (p = 1.31×10^{-39}) and iNs (p = 3.69×10^{-36}) (Figure 1C).

Gene set enrichment analysis highlighted differential molecular consequences to *MEF2C* deletion in NSCs and iNs. Haploinsufficiency of *MEF2C* in NSCs led to dysregulation of genes involved in developmental processes including developmental pattern specification, organ morphogenesis, neurogenesis, and neuron differentiation (Figure 1D). Additionally, DEGs resulting from homozygous loss of *MEF2C* in NSCs were enriched for LoF-constrained genes and gene sets associated with NDDs from exome sequencing.[22] These LoF and NDD-associated genes are heavily weighted toward genes that display high levels of expression during early neurodevelopment and experience strong negative selection against gene disruptive mutations (Figure 1D). In contrast to NSCs, DEGs identified in iNs were significantly enriched for DEGs observed in forebrain excitatory neurons of an *Mef2c* knockout mouse model published by Harrington et al.[50] (Figure 1D). Additionally, DEGs observed in DEL[het] iNs were enriched for functional terms such as neurogenesis and neuronal differentiation. Homozygous loss of *MEF2C* in iNs also yielded DEGs that were enriched for synaptic genes (Figure 1D). When comparing these results to data from the BrainSpan project,[53] which identified neural-activity-defining gene co-expression modules with 146 samples from 21 fetal to infant developing brains, iN DEGs were enriched for BrainSpan modules associated with synaptic transmission, synaptic maturation, and genes defined as MEF2C-binding targets[53] (modules M13 and M17; Figure 1D). These findings replicated with co-expression modules from a more recent and larger study of 1,230 samples from 48 brains in psychENCODE.[54] We observed the module from Li et al.[54] (ME37), which includes *MEF2C*, was enriched for DEGs from DEL[het] iNs (Figure 1D). This module from the psychENCODE study demonstrated expression patterns associated with neuron development and was enriched for genes that converged on associations with neurodevelopmental and neuropsychiatric disorders.

Overall, the biological pathways and processes shared across DEGs from NSCs and iNs were strongly enriched for neuronal terms including neurogenesis, neuron differentiation, and regulation of cell differentiation and specifically neuron differentiation (FDR < 0.1). Intriguingly, we also observed that DEGs identified in both NSCs and iNs were enriched for AACTTT- and FOXJ2-binding motifs (FDR < 0.1). The AACTTT-binding motif has previously been associated with the promoter of *MEF2C* and enriched at the promoters of genes involved in neurodevelopment and muscle development.[65,66] The FOXJ2-binding motif has similarly been shown to recruit transcriptional activators that function in early developmental stages.[67] Taken together, these data suggest that the expression signatures associated with LoF mutations of *MEF2C* are consistent with perturbations to highly constrained genes broadly involved in transcriptional regulation during early neural development as well as genes that display distinct expression patterns in later developmental time points and impact neuronal communication and synaptic functions.

Altered co-expression of genes in neurodevelopmental and synaptic pathways associated with deletion of *MEF2C*

We next established modules of co-expressed genes in NSCs and iNs by using WGCNA (Figure 2). In NSCs, four co-expression modules had an eigengene that correlated significantly with *MEF2C* dosage: violet (p = 2.4×10^{-7}), bisque4 (p = 1.4×10^{-6}), yellow4 (p = 2.1×10^{-4}), and darkslateblue (p = 2.9×10^{-5}) (Figures 2A, 2B, and 2E). Yellow4 genes, which showed increased expression with
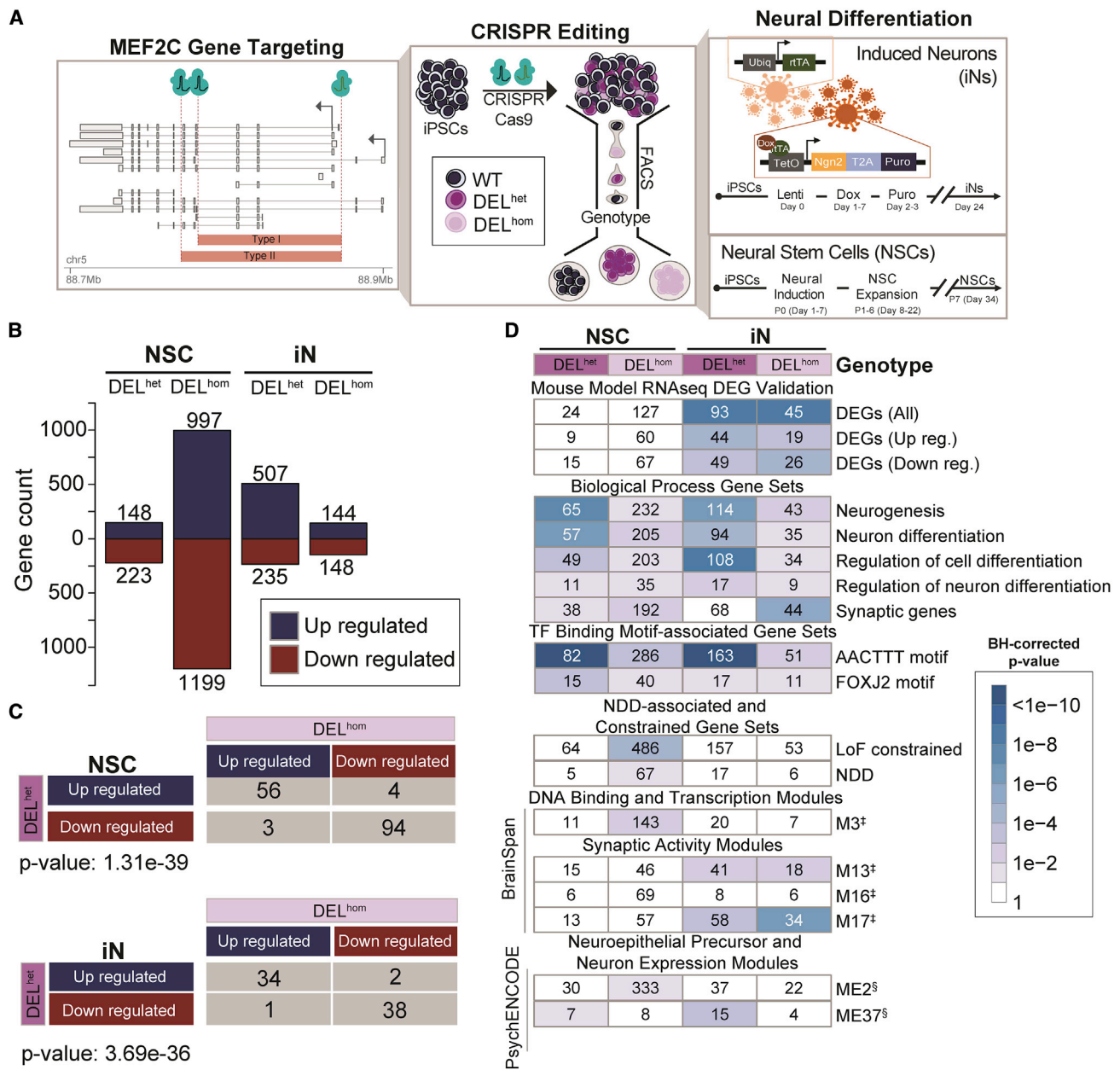
Figure 1. *MEF2C* deletion results in differential expression of genes enriched for neurodevelopmental and synaptic processes

(A) Schematic representation of *MEF2C* transcripts and location of CRISPR guide RNAs that introduced two independent deletions (type I and type II) into human induced pluripotent stem cells (hiPSCs). Fluorescence-activated cell sorting (FACS) was performed, followed by screening of individual clones that identified both heterozygous (DEL^het) and homozygous (DEL^hom) deletions of *MEF2C* and unedited wild-type (WT) clones that were exposed to identical CRISPR targeting. Neural differentiation was then conducted followed by RNA-seq. CRISPR deletion breakpoints of *MEF2C* are shown relative to transcripts with >1TPM expression in ≥1 GTEx tissue. Arrows represent positions of canonical transcription start sites of *MEF2C*.

(B) Differentially expressed genes (DEGs) per cell type and genotype.

(C) DEG concordance analysis by cell type and genotype group with statistical significance (p value) of shared directionality calculated with Fisher's exact test.

(D) DEG enrichment for gene sets and modules associated with neurological phenotypes, synaptic activity, and *MEF2C* function in prior studies. Mouse model RNA-seq DEG validation from Harrington et al.;[50] biological processes gene sets and TF-binding motif gene sets from GSEA msigDB;[48,63] synaptic genes from Syngo v1.1;[51] *MEF2C* targets from ENCODE project (ChIPseq in Epstein-Barr virus [EBV]-transformed lymphoblastoid B-cell lines [LCLs]);[52] LoF-constrained genes from gnomAD;[64] genes associated with neurodevelopmental disorders (NDDs) from analyses in Fu et al.;[22] DNA-binding and transcription modules and synaptic activity modules from Parikshak et al.[53] (‡); neuroepithelial precursor and neuron expression modules (§) from Li et al.[54]

MEF2C loss, were notably enriched for processes of heart morphogenesis[13,68–70] and RHO GTPase activation[71] (FDR < 0.1), both of which have been described previously

in relation to *MEF2C* function. Furthermore, we also considered co-expression modules with an eigengene that correlated with DEL^het *MEF2C* loss alone. Module
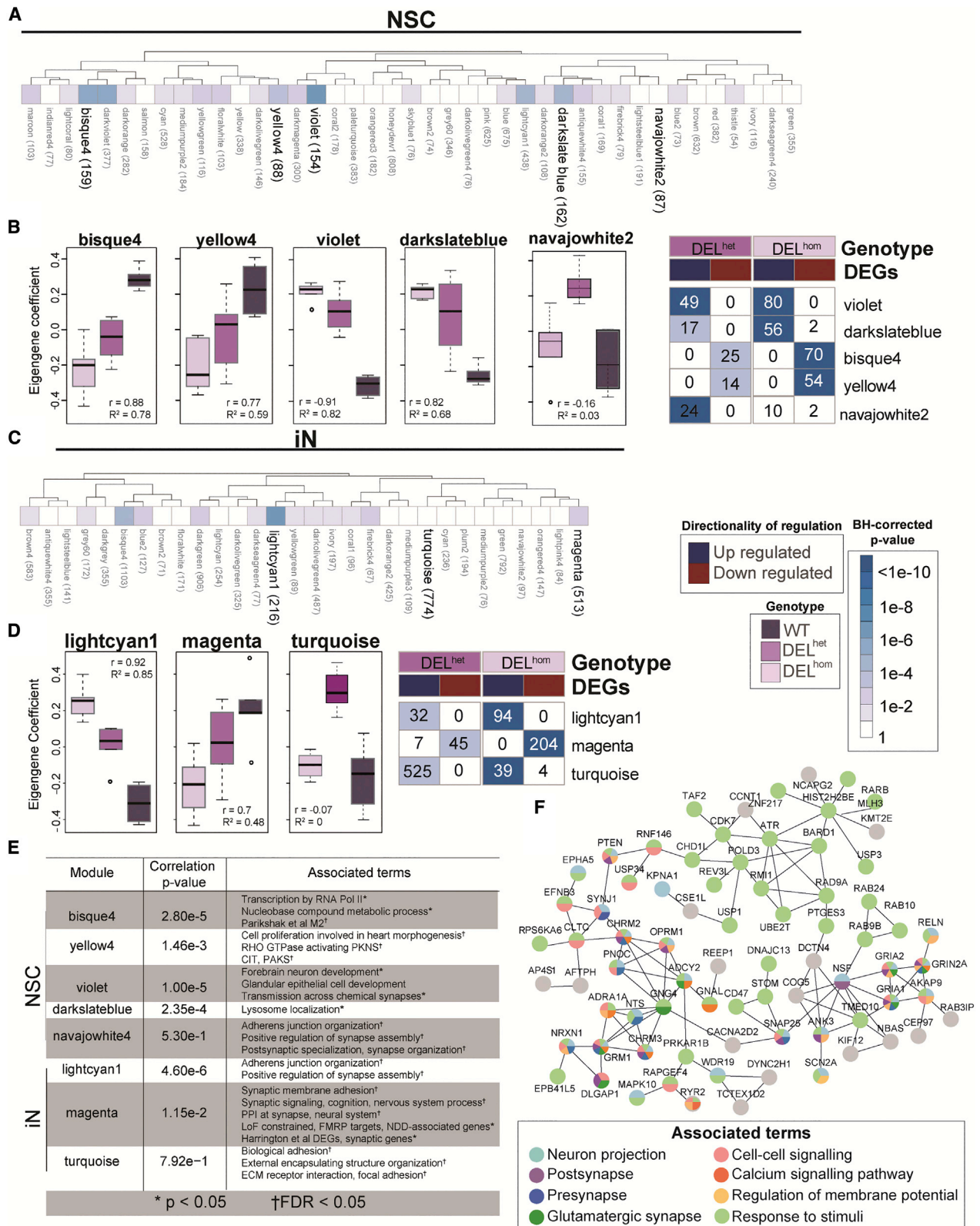
Figure 2. Co-expression modules enriched for constrained genes and synaptic activity are correlated with *MEF2C* disruption in neuronal cells

(A–F) Dendrogram displaying all modules identified from weighted gene co-expression network analysis (WGCNA). Modules demonstrating statistically significant correlation with *MEF2C* genotype (i.e., allelic dosage) are bolded for neural stem cells (NSCs; A) and glutamatergic induced neurons (iNs; C), respectively, with p value of correlation significance indicated by color shade. Boxplots

navajowhite2 ($p = 5.30 \times 10^{-1}$) contained genes significantly up-regulated only in DEL[het] NSCs and was enriched for terms related to synapse assembly and organization.

Co-expression analysis in iNs isolated two modules whose eigengenes significantly correlated with *MEF2C* dosage, lightcyan1 ($p = 1.5 \times 10^{-7}$) and magenta ($p = 1.9 \times 10^{-3}$), and one module, turquoise, with neuronal function and only affected by single copy edit of *MEF2C* ($p = 7.9 \times 10^{-1}$) (Figures 2B, 2C, and 2E). Genes within module lightcyan1 were enriched for DNA damage repair-associated nucleotide patch replacement (FDR < 0.1). In addition to having an essential role in cardiac and neurodevelopment, previous reports have also described *MEF2C* as serving lineage-specific roles in regulation of DNA damage repair.[72,73] The genes co-expressed in the magenta module revealed a far greater emphasis on alterations to synaptic functions, being enriched for synaptic membrane adhesion, synaptic signaling, and PPI at the synapse (FDR < 0.1). The encoded proteins (n = 513) were mapped to a PPI network via StringDB[74,75] in Cytoscape,[76–78] resulting in a network with 150 members (confidence score > 0.7, evidence = experimental/database, PPI enrichment $p < 1 \times 10^{-16}$). The proteins from 76 genes contained within module magenta formed a network associated with neuronal and synaptic terms (Figure 2F). Module magenta also included genes associated with monogenic forms of epilepsy and other NDDs, such as *GRIN2A*, *SCN2A*, and *GRIA2*, providing evidence of molecular convergence for these genotypically distinct but strongly synaptic-activity-associated disease genes.[79–81]

MEF2C direct disruption yields changes to synaptic firing and synchrony in human neural models as measured by MEA

Given the strong transcriptional changes associated with deletion of *MEF2C* in hiPSC-derived neurons that converged on synaptic activity, we sought to functionally validate this association by defining electrophysiological changes in neurons via MEA (Figure 3; supplemental methods, section 2.6; Figures S5–S7). We differentiated heterozygous and homozygous *MEF2C* lines and matched controls to iNs and observed a statistically significant (on the basis of t test) down-regulation of synaptic activity in iNs. We observed statistically significant reductions in firing rate relative to wild type for both DEL[het] (26%, $p = 1.4 \times 10^{-5}$) and DEL[hom] (31%, $p = 1.3 \times 10^{-2}$) (Figure 3A). We also observed statistically significant reductions to spike count relative to wild type for both DEL[het] (17%, $p = 6.7 \times 10^{-3}$) and DEL[hom] (48%, $p = 5.1 \times 10^{-5}$) (Figure 3B). Additionally, we observed statistically significant reductions to synchrony, a measure of uniformity of neuronal firing bursts, relative to wild type

for both DEL[het] (32%, $p = 7.1 \times 10^{-3}$) and DEL[hom] (73%, $p = 9.6 \times 10^{-9}$) (Figure 3C). While we observed clear changes in firing rate, neither DEL[het] ($p = 0.68$) nor DEL[hom] ($p = 0.30$) loss of *MEF2C* resulted in significant changes to network burst oscillation (Figure 3D). These data provided a complementary measure of *MEF2C* direct disruption resulting in altered synaptic activity.

Dissecting 3D chromatin topology and regulatory interactions within the 5q14.3 locus

Our prior analyses from whole-genome sequencing of individuals with NDDs harboring BCAs,[38] and other recent studies,[3,82–87] have suggested that *cis*-regulatory disruption by noncoding SVs may underlie NDD phenotype association within the 5q14.3 locus beyond direct LoF *MEF2C* mutation. Collectively, these seven studies have reported CNV and BCA breakpoints 200–500 kb distal to *MEF2C* in 13 distinct cases presenting with phenotypes consistent with *MEF2C* haploinsufficiency such as NDD, epilepsy, and hypotonia. As a result, enhancer-promoter decoupling by disruption to 3D chromatin organization has emerged as a mechanistic hypothesis for indirect *MEF2C* disruption. We therefore performed a comprehensive and systematic dissection of the TAD and loop organization of the 5q14.3 region in human neural models. From analyses of existing 2D enhancer elements, *MEF2C* chromatin interactions in NSC and iN models as determined via UMI-4C,[88] as well as 3D elements such as boundaries and structural protein ChIP annotations (CTCF and SMC3) from published datasets,[31,89] we defined both 2D and 3D elements with evidence for a role in *MEF2C* regulation (supplemental methods, section 3.1; Figures S8 and S9). We then sought to determine the overarching 3D chromatin architecture responsible for orchestrating gene-enhancer interactions by generating an allelic series of deletions targeting 2D and 3D functional elements within the 5q14.3 locus (Figure 4).

We annotated topological structures from Epstein-Barr virus (EBV)-transformed lymphoblastoid B-cell lines (LCLs) by using Hi-C data and integrated CTCF- and SMC3-binding sites indicated by LCL ChIP-seq.[31,89] We confirmed the presence of *MEF2C* in the loop structure identified in LCLs in our NSC and iN models by profiling interactions from the *MEF2C* promoter by using UMI-4C (Figures 4 and S11). Dual guide CRISPR-Cas9-based genome editing guides were then designed to engineer a series of deletions of the candidate 3D elements as outlined in Figure 4. We targeted deletion of four genomic sites, including the proximal and distal boundaries of the *MEF2C*-containing loop as the key experimental edits (referred to as "proximal boundary" and "distal boundary," respectively), and two "negative control" edits, namely the

demonstrating each eigengene's coefficient of correlation per genotype per co-expression module, and corresponding heatmaps, shown for NSCs (B) and iNs (D). (E) Associated terms with significant enrichment per highlighted module. (F) The PPI network of highly connected genes (n = 76) of the magenta module with functional annotations. The node colors indicate the functional classes for each protein and the edge represents interaction.
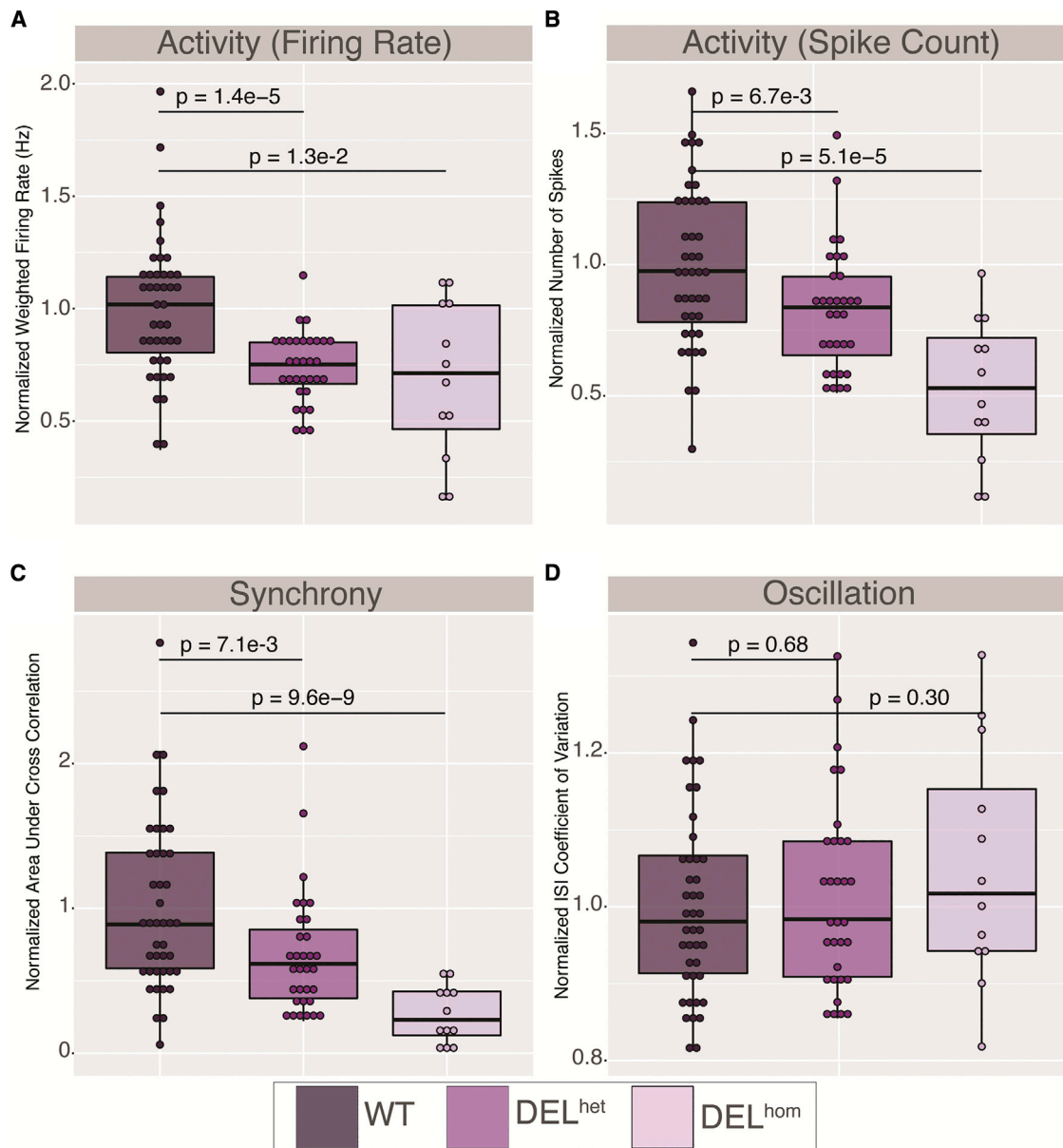
Figure 3. Reduced synaptic activity and synchrony in heterozygous (DEL^het) and homozygous (DEL^hom) deletions of *MEF2C* in neurons via multi-electrode array

Each datapoint represents a single replicate well. Each resultant measurement was normalized per well against the wild-type (WT) mean per plate and normalized data points from two replicate plates plotted.

(A) Normalized weighted mean firing rate (Hz) (firing rate).

(B) Normalized number of spikes (spike count).

(C) Normalized area under cross correlation (synchrony).

(D) Normalized ISI (interspike interval) coefficient of variation (oscillation). p values were calculated via t test against normalized wells per genotype.

boundary of the TAD adjacent to *MEF2C* ("adjacent TAD"), and the genomic sequence spanning the *MEF2C*-containing and adjacent TAD with no occupied CTCF-binding sites in 133 cell/tissue samples from ENCODE ("separator"). We focused on this *MEF2C* loop structure as opposed to the larger TAD given that it was largely cell type invariant in both the above resources and additional cell types as well as the strength of contact with *MEF2C* and its higher resolution map of the 3D organization encompassing the *MEF2C*-relevant enhancers (supplemental methods, section 3.1; Figures S8–S10). Differentiated hiPSC-derived iN and NSC CRISPR models were generated for each of these four deletion models with six replicates per DEL^het and DEL^hom genotype as well as six control clones that were exposed to the CRISPR conditions but not edited (as described in material and methods). Differentiation of these hiPSCs established 204 individual neuronal lines representing systematic disruption to functional elements within the 5q14.3 locus (supplemental methods, section 3; Figures S15–S22).
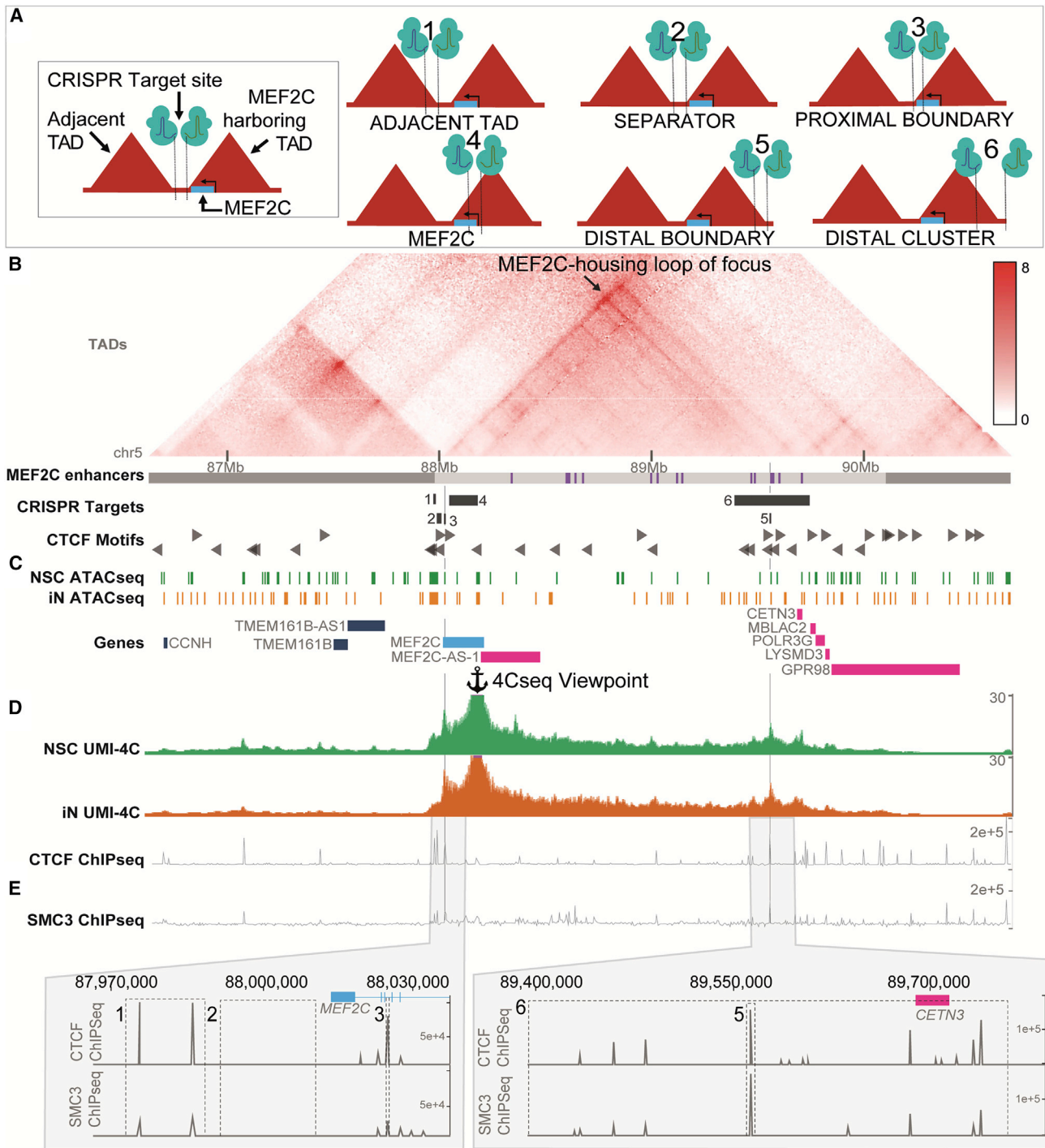
Figure 4. Design of CRISPR deletion allelic series
(A) Depiction of CRISPR targets relative to *MEF2C* and local 3D structures.
(B) Knight-Ruiz normalized Hi-C map from GM12878 wild-type EBV-transformed lymphoblastoid B-cell lines (LCLs) shown.[31] Local topologically associating domain (TAD) annotations[89] and putative *MEF2C* enhancers[88] denoted as grey and purple bars, respectively. Black arrow within the Hi-C map and vertical grey lines highlight the *MEF2C*-housing loop of focus targeted in this study.
(C) Open chromatin regions identified by ATAC-seq in wild-type neural stem cells (NSCs) and glutamatergic induced neurons (iNs).
(D) Aggregate contacts from UMI-4C in wild-type NSCs and iNs shown relative to the viewpoint within the MEF2C promoter.
(E) Deletion positions of 3D topology boundaries guided by ChIP-seq for structural proteins CTCF and SMC3 in GM12878 LCLs.

Distal boundary deletion does not result in marked change to *MEF2C* expression

We observed that DEL^het and DEL^hom of the separator and adjacent TAD boundary deletions resulted in no substantial changes in *MEF2C* expression or to contacts between the *MEF2C* promoter and published enhancers of *MEF2C*[88] based on UMI-4C, as expected (Figure 5; supplemental methods, section 3.8; Figures S23, S24, S27, and S28).
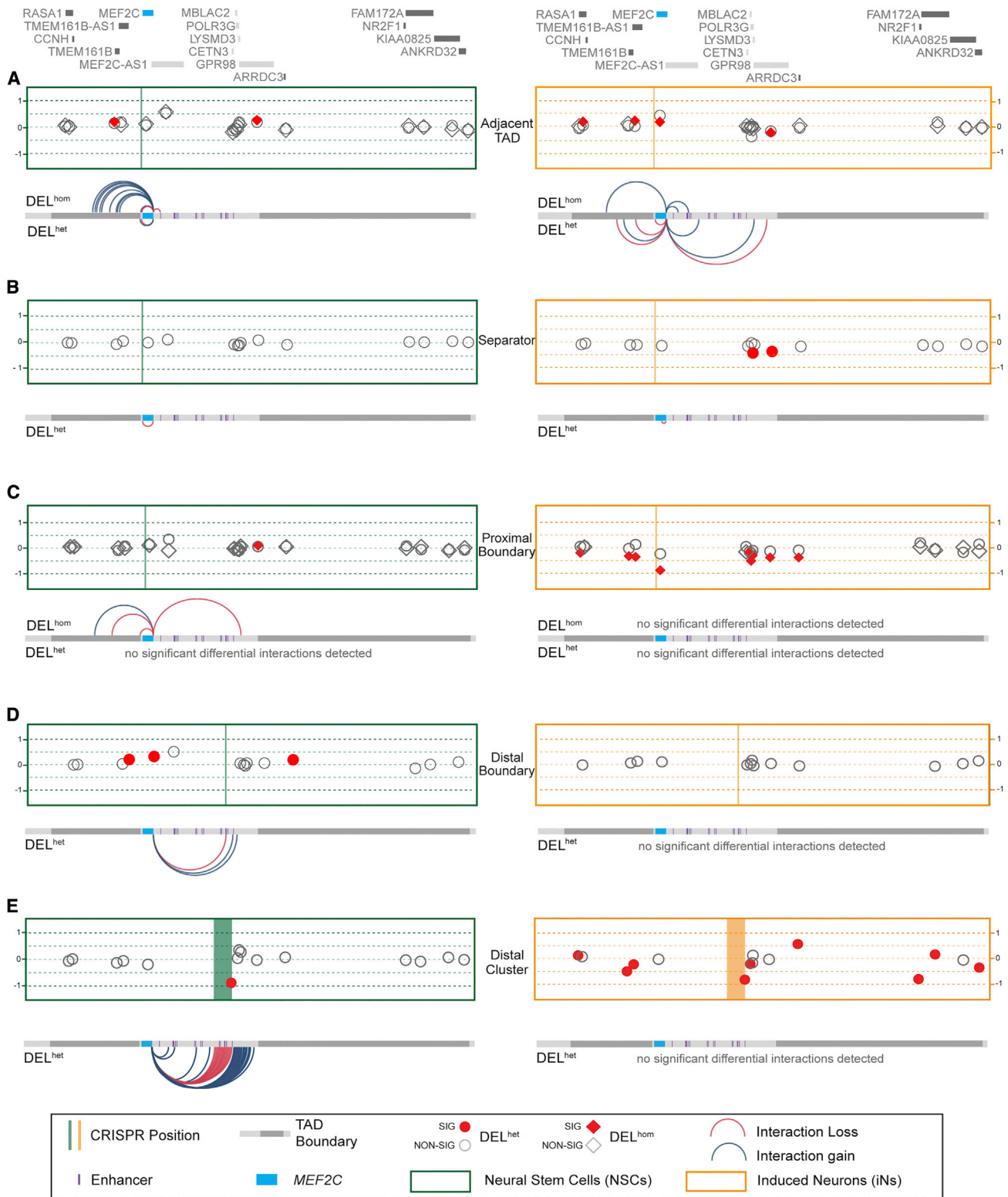
Figure 5. *MEF2C* expression and long-range contact changes following CRISPR allelic series

(A–E) In (A)–(E), the Y axis displays log$_2$ fold change of differential expression for *MEF2C*. We also show 15 genes with detectable expression that are localized to either the topologically associating domain (TAD) encompassing *MEF2C* or one of the proximal or distal TADs. The significantly differentially expressed genes (locally corrected false discovery rate [FDR] < 0.1) in neural stem cells (NSCs) and glutamatergic induced neurons (iNs) are shown in red and the genes that are not differentially expressed are outlined in grey. Differential expression of each gene is annotated by a circle for heterozygous deletions (DEL^{het}) and a diamond for homozygous deletions (DEL^{hom}). Position of CRISPR deletion annotated by vertical line. Differential contacts with the *MEF2C* promoter in each CRISPR line relative to matched wild type indicated by curved lines (Figures S26–S31). Lines included for significant contact changes with FDR < 0.1 based on a sliding window of 5 kb with 200 bp step. (A)–(E) represent individual CRISPR edits as labeled in the figure.

The distal boundary deletion served to directly test the necessity of 3D chromatin topology for robust expression of *MEF2C*.[3,38,82–85] Surprisingly, deletion of this site resulted in no change in MEF2C protein accumulation and a slight increase (25% compared to wild type) in mRNA expression for DEL[het] in NSCs ($\log_2$FC = 0.33; FDR < 0.1 when correcting for multiple testing within the TAD, Figures 5 and S24). Aside from *MEF2C*, we also considered expression of genes expressed in NSCs or iNs that were located within either the *MEF2C*-containing TAD, the TAD directly proximal, or the TAD directly distal, which we refer to as herein as "local genes," by using TADs as defined by Dixon et al.[89] Fifteen genes (not including *MEF2C*) met this criterion for local gene inclusion in NSCs, while 14 were considered in iNs given that *MEF2C-AS1* was not expressed in this cell type. We observed no altered expression of any local genes aside from *MEF2C* in distal boundary deletion NSCs. To further explore this finding, we employed allele-specific UMI-4C anchored at the *MEF2C* promoter (Figure 5; supplemental methods, Section 3.8; Figure S30). These analyses identified an increase in significant (FDR < 0.1) contacts between the *MEF2C* promoter and two separate 6 kb windows harboring CTCF-binding sites immediately distal to the deletion position, suggesting CTCF motif redundancy may buffer deletions to canonical 3D boundary elements, preventing strong dysregulatory effects. In DEL[het]-matched iNs with distal boundary deletions, no significant expression or contact changes were observed for *MEF2C* or any other local genes. We note that we only considered DEL[het] disruption of the distal boundary given that DEL[hom] lines were not recovered from our editing workflow.

To further evaluate this largely negative result, we tested the hypothesis of regulatory element redundancy buffering against pronounced expression effects on *MEF2C*. We did so by deleting what we referred to as the distal cluster, a 354 kb region that includes six annotated enhancers (e11–e16), five directly oriented CTCF-binding site motifs, the distal boundary, and one local gene, *CETN3* (Figure 4). We note that the generation of this large CRISPR deletion was performed directly in NSCs (by comparison to the hiPSC stage prior to differentiation for all other models) and is thus a technically distinct validation experiment rather than directly comparable to the models in the initial hypothesis test. Nonetheless, in these analyses we observed no significant differential expression of *MEF2C* upon DEL[het] deletion of the distal cluster region when compared to matched wild types in either NSCs or NSC-derived iNs (Figures S24 and S25). Considering UMI-4C data from the viewpoint of the *MEF2C* promoter in these lines, we observed a significant (FDR < 0.1) increase in contacts with four sites within 5q14.3 alongside a contiguous increase with the 320 kb region immediately distal to the deleted region in NSCs (Figures 5 and S31). Considering local genes not directly disrupted by the deletion, we observed a cascade of significant (FDR < 0.1) dysregulation of 8/15 genes in 5q14.3 locus in iNs, with no genes significantly dysregulated in matched NSCs. Together, these analyses suggest that deletion of the distal boundary of the *MEF2C*-encompassing loop is insufficient to indirectly dysregulate this NDD-associated gene.

Proximal boundary deletion yields reduction of *MEF2C* expression and synaptic activity in iNs

In contrast to the weak or largely negative results observed for deletion of the distal boundary, deletion of the proximal boundary, which is located in an intron of *MEF2C*, had marked effects on the gene's expression that appeared to be genotype and cell type dependent. NSCs harboring DEL[het] or DEL[hom] of the proximal boundary did not display differential expression of *MEF2C*, though protein accumulation was significantly reduced in DEL[hom] (49% relative to controls; p = 5.7×10^{-4}, Figures S23 and S24). These DEL[hom] NSCs also displayed differential contacts with the *MEF2C* promoter at four sites, three of which were significantly increased and one significantly decreased (locally corrected FDR < 0.1) (Figures 5 and S29). Moreover, homozygous deletion of the proximal boundary in iNs resulted in pronounced down-regulation of *MEF2C*, five genes localized to the *MEF2C*-containing TAD, and three genes within the TAD proximal to the *MEF2C*-containing TAD (locally corrected FDR < 0.1; Figure 5). This consistent down-regulation thus extended up to 3 Mb from the site of the deletion and was also dosage dependent, as DEL[hom] deletion resulted in significantly reduced expression compared to unedited and DEL[het] cells (Figure 5). These positional effects were particularly strong for *MEF2C*, and DEL[hom] deletion largely recapitulated the reduction observed with heterozygous direct gene deletion (i.e., 45% reduction, locally corrected FDR = 1.9×10^{-9}, genome-wide FDR = 6.3×10^{-8}) (Figure 5).

We next explored transcriptional and functional commonalities between direct *MEF2C* disruption and indirect expression reduction by proximal boundary deletion. We observed shared DEGs from direct *MEF2C* disruption in both NSCs and iNs with proximal boundary deletion (Figure 6). We also observed shared functional pathways in iNs related to synaptic activity, neurodevelopment, and neural differentiation between these distinct coding and noncoding functional mutations (Figure 6). The proximal boundary DEL[hom] and direct *MEF2C* deletion iN DEGs also shared significant enrichment of terms such as axon development alongside sharing an enrichment for genes with promoter containing the sequence motif AACTTT, a binding motif in genes involved in neurodevelopment and muscle development.[65,66] Given our demonstration of shared neuronal pathways between direct *MEF2C* deletion and proximal boundary deletion lines, we next tested whether this noncoding regulatory proximal boundary deletion replicated the synaptic deficits observed with *MEF2C* deletions. From these analyses, we observed a similarly strong reduction in synaptic activity for both DEL[het] and DEL[hom] iNs when compared to
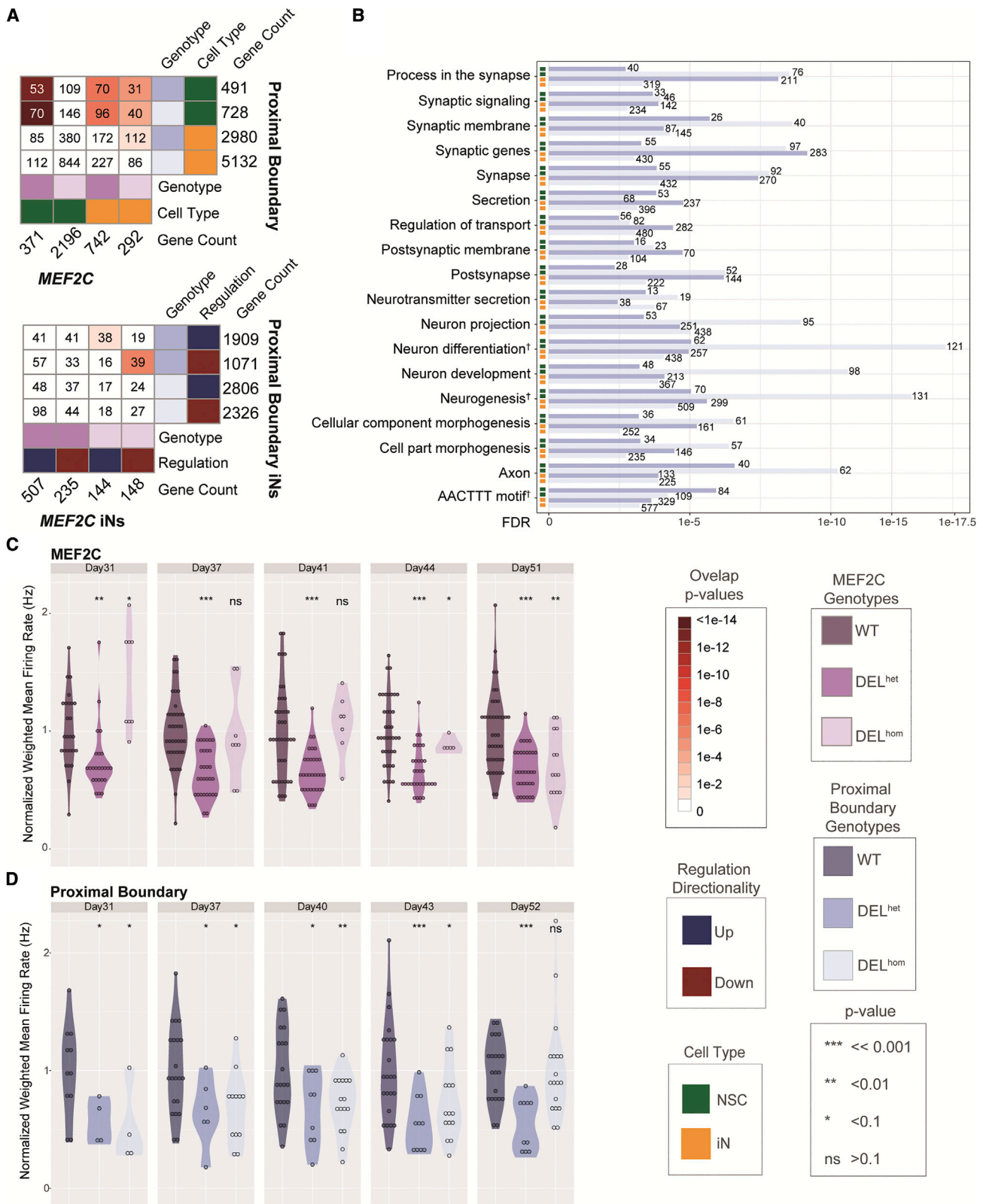
Figure 6. Proximal boundary disruption yields disruption of genes involved in neuron differentiation and alters synaptic activity

(A) Differentially expressed genes (DEGs) comparison between lines harboring deletion of *MEF2C* and the proximal boundary deletion in neural stem cells (NSCs) and glutamatergic induced neurons (iNs)(top: both NSCs and iNs, bottom: iNs only).

(B) Functional enrichment of proximal boundary DEGs. Terms that are shared in iNs and NSCs harboring heterozygous and homozygous *MEF2C* deletions are also noted. Normalized weighted mean firing rate over time as measured by multi-electrode array (MEA) shown for iNs harboring *MEF2C* deletions (C) and iNs with proximal boundary deletions (D), respectively. The p values were calculated via t test against the wild types (WTs).

matched wild-type clones over the differentiation time course measurements (Figure 6; Day 31–day 43). The pattern and significance detected for spike number and number of bursts over time was also consistent with the *MEF2C* deletion MEA time course experiment, suggesting a reproducible synaptic phenotype associated with both direct deletion and noncoding regulatory alterations to the *MEF2C* locus (supplemental methods, section 3.8; Figures S32–S34).

Discussion

We present an initial survey of the transcriptional and electrophysiological consequences of *MEF2C* gene deletion and indirect regulatory changes introduced by alterations to 5q14.3 TAD and chromatin loop topology in human-derived *in vitro* neural models. Direct LoF mutations (PTVs, deletions, translocations) within *MEF2C* have repeatedly been associated with NDD risk.[1,2,6,8,9,83,84,90–93] A variety of murine knockout models, including conditional knockout of *MEF2C* in varying neural cell types and developmental time points, have collectively suggested a role for *MEF2C* in neuronal function,[13,14,16,50] but no studies have evaluated *MEF2C* LoF mutations in human-derived cell lineages. In the study presented here, we engineered an allelic series of CRISPR-generated mutations within *MEF2C* and its putatively regulatory 3D functional elements and demonstrated that both direct and indirect alterations to *MEF2C* expression converge on themes related to neurodevelopment and synaptic activity.

Recently, specific studies that have focused on the knockout of *SMC3* in human cell models,[29] genome rearrangements in *Drosophila*,[36] and TAD disruption at the *Shh* locus[94] have demonstrated the uncoupling of regulatory changes associated with gene expression and alterations to long-range chromatin contacts. Our data further support those studies, as we observed alterations to 3D topological organization that occur without concomitant changes in gene expression. These demonstrations are in contrast to the hallmark examples of TAD disruption underlying dysregulation of a gene associated with a human disease phenotype.[31,33–35] Most of the CRISPR models targeting 2D and 3D noncoding element deletions generated in this study demonstrated modest or no functional impact on expression of *MEF2C* and genes encompassed within the adjacent TADs. Furthermore, most CRISPR models also did not result in major changes to long-range contacts with the *MEF2C* promoter. We did note some robust changes in contact patterns from UMI-4C conducted in our NSC CRISPR lines, but most observed differential contacts did not engage previously validated enhancers of *MEF2C*. These findings further illustrate the complexity associated with the dynamic interactions that result from SV alterations of 3D topology and regulation of gene function.

Our approach weighted elements contributing to 3D genome organization given the previous reports highlighting TAD disruption as a putative indirect cause of *MEF2C* haploinsufficiency.[38,83] In our most recent WGS study of 406 individuals with developmental disorders that harbored a BCA, as well as 304 BCAs from control individuals, the 5q14.3 locus continues to display a genome-wide significant enrichment of noncoding SV breakpoints that localize distal to *MEF2C*. The homozygous proximal boundary deletion caused a 2-fold reduction of *MEF2C* expression that was comparable to haploinsufficiency resulting from heterozygous deletion. The absence of a coding SNP within *MEF2C* prevented the determination of whether up-regulation of *MEF2C* on the wild-type allele prevented observed differential expression in heterozygous deletion of proximal boundary lines. This region has been recently reported as a *cis*-regulatory site that was demonstrated to reduce *MEF2C* expression following CRISPR interference (CRISPRi) in K562 cells.[95] The shared enrichment of gene sets related to neurogenesis and neuronal differentiation between both proximal boundary and *MEF2C* DEGs demonstrates transcriptome dysregulation by both direct and indirect *MEF2C* disruption that converge upon biological processes of relevance to NDDs. We also observe significant overlap between indirect disruption of *MEF2C* by proximal boundary deletion in NSCs and direct *MEF2C* disruption in iNs, suggesting dysregulatory effects may involve temporal or cell-type-specific dysregulation. Furthermore, the shared enrichment of genes with AATCCC-binding motifs within their promoters, which was previously associated with genes involved in neuronal differentiation, including *MEF2C*, alongside the comparable reductions in synaptic activity as measured by MEA, suggest shared functional consequences from direct and indirect *MEF2C* disruption. However, the deletion of the distal boundary did not recapitulate these results. While the data are therefore unambiguous of a localized enrichment of disease-associated noncoding SV breakpoints spanning the *MEF2C*-containing 3D organization, the models that displayed the greatest transcriptional and functional consequences were not those that were predicted *a priori* on the basis of the localization of the SV breakpoints alone. The noncoding regulatory mechanisms that govern NDD risk in this region thus remain elusive and appear to be cell type and genotype specific. The deletions introduced here do not result in the same degree of genome topological rewiring as would be predicted from the translocations and inversions observed in the BCA cases, and the functional changes observed are not consistent across cell types. Similarly, in an NDD-affected individual with a *de novo* inversion upstream of MEF2C, the TAD structure is disrupted in LCL without any expression change for *MEF2C*.[96] These analyses illustrate the highly complex regulatory architecture of alterations to chromatin topology and emphasize the significant challenges for computational prediction of the regulatory features of SVs.[97–99]

We present a comprehensive CRISPR-engineered isogenic allelic series of *MEF2C* disruption in human-derived *in vitro*

models and functional characterization of resultant transcriptional and electrophysiological effects. These studies also uniquely dissect the parallel consequences of direct and indirect alterations to *MEF2C* by *cis*-regulatory disruption, revealing that some noncoding mutations can recapitulate synaptic deficits and transcriptional signatures observed from direct deletion of this gene underlying the well-established 5q14.3 microdeletion syndrome. While direct deletion of *MEF2C* revealed functional changes in human neurons that were consistent with previous studies in mouse models,[14–17,50] our results following SV alteration to 3D organization of 5q14.3 underscore the complexity of regulatory interactions at this locus and more broadly in defining the features associated with the functional impact of noncoding SVs genome wide. These data clearly demonstrate that alteration to annotated boundaries of 3D regulatory architecture encompassing established human disease genes is insufficient evidence to presume alterations to gene regulation or phenotypic impact. Future *in silico*, *in vitro*, and *in vivo* studies targeting more loci and classes of SVs with designs that either recapitulate case rearrangements or are agnostic to regulatory element type will be necessary to further expand these findings into systematic analysis of the features associated with 3D genome architecture and noncoding disease association.

Data and code availability

Data for the study are available at NCBI GEO database with accession number GEO: GSE204778. Codes for specific analyses are available upon request.

Supplemental information

Supplemental information can be found online at https://doi.org/10.1016/j.ajhg.2022.09.015.

Declaration of interests

M.E.T. receives research funding and/or reagents from Levo Therapeutics, Microsoft Inc, and Illumina Inc. K.M. initiated employment with Tornado Bio during the writing of this manuscript and is at present an employee of the company. J.F.G. is a founder and member of the scientific advisory board of Triplet Therapeutics, Inc., and has been a paid consultant to Biogen, Inc., Pfizer, Inc., and Wave Biosciences, Inc.

References

1. Engels, H., Wohlleber, E., Zink, A., Hoyer, J., Ludwig, K.U., Brockschmidt, F.F., Wieczorek, D., Moog, U., Hellmann-Mersch, B., Weber, R.G., et al. (2009). A novel microdeletion syndrome involving 5q14.3-q15: clinical and molecular cytogenetic characterization of three patients. Eur. J. Hum. Genet. *17*, 1592–1599.

2. Cardoso, C., Boys, A., Parrini, E., Mignon-Ravix, C., McMahon, J.M., Khantane, S., Bertini, E., Pallesi, E., Missirian, C., Zuffardi, O., et al. (2009). Periventricular heterotopia, mental retardation, and epilepsy associated with 5q14.3-q15 deletion. Neurology *72*, 784–792.

3. Zweier, M., Gregor, A., Zweier, C., Engels, H., Sticht, H., Wohlleber, E., Bijlsma, E.K., Holder, S.E., Zenker, M., Rossier, E., et al. (2010). Mutations in MEF2C from the 5q14.3q15 microdeletion syndrome region are a frequent cause of severe mental retardation and diminish MECP2 and CDKL5 expression. Hum. Mutat. *31*, 722–733.

4. Le Meur, N., Holder-Espinasse, M., Jaillard, S., Goldenberg, A., Joriot, S., Amati-Bonneau, P., Guichet, A., Barth, M., Charollais, A., Journel, H., et al. (2010). MEF2C haploinsufficiency caused by either microdeletion of the 5q14.3 region or mutation is responsible for severe mental retardation with stereotypic movements, epilepsy and/or cerebral malformations. J. Med. Genet. *47*, 22–29.

5. Carr, C.W., Zimmerman, H.H., Martin, C.L., Vikkula, M., Byrd, A.C., and Abdul-Rahman, O.A. (2011). 5q14.3 neurocutaneous syndrome: a novel continuous gene syndrome caused by simultaneous deletion of RASA1 and MEF2C. Am. J. Med. Genet. *155A*, 1640–1645.

6. Bienvenu, T., Diebold, B., Chelly, J., and Isidor, B. (2013). Refining the phenotype associated with MEF2C point mutations. Neurogenetics *14*, 71–75.

7. Wang, J., Zhang, Q., Chen, Y., Yu, S., Wu, X., Bao, X., and Wen, Y. (2018). Novel MEF2C point mutations in Chinese patients with Rett (-like) syndrome or non-syndromic intellectual disability: insights into genotype-phenotype correlation. BMC Med. Genet. *19*, 191.

8. Novara, F., Rizzo, A., Bedini, G., Girgenti, V., Esposito, S., Pantaleoni, C., Ciccone, R., Sciacca, F.L., Achille, V., Della Mina, E., et al. (2013). MEF2C deletions and mutations versus duplications: a clinical comparison. Eur. J. Med. Genet. *56*, 260–265.

9. Nowakowska, B.A., Obersztyn, E., Szymańska, K., Bekiesińska-Figatowska, M., Xia, Z., Ricks, C.B., Bocian, E., Stockton, D.W., Szczałuba, K., Nawara, M., et al. (2010). Severe mental retardation, seizures, and hypotonia due to deletions of MEF2C. Am. J. Med. Genet. B Neuropsychiatr. Genet. *153B*, 1042–1051.

10. Cesaretti, C., Spaccini, L., Righini, A., Parazzini, C., Conte, G., Crosti, F., Redaelli, S., Bulfamante, G., Avagliano, L., and Rustico, M. (2016). Prenatal detection of 5q14.3 duplication including MEF2C and brain phenotype. Am. J. Med. Genet. *170A*, 1352–1357.

11. Novara, F., Beri, S., Giorda, R., Ortibus, E., Nageshappa, S., Darra, F., Dalla Bernardina, B., Zuffardi, O., and Van Esch, H. (2010). Refining the phenotype associated withMEF2Cha-ploinsufficiency. Clin. Genet. *78*, 471–477.

12. Tonk, V., Kyhm, J.H., Gibson, C.E., and Wilson, G.N. (2011). Interstitial deletion 5q14.3q21.3 with MEF2C haploinsufficiency and mild phenotype: When more is less. Am. J. Med. Genet. *155A*, 1437–1441.

13. Lin, Q., Schwarz, J., Bucana, C., and Olson, E.N. (1997). Control of mouse cardiac morphogenesis and myogenesis by transcription factor MEF2C. Science *276*, 1404–1407.

14. Flavell, S.W., Cowan, C.W., Kim, T.K., Greer, P.L., Lin, Y., Paradis, S., Griffith, E.C., Hu, L.S., Chen, C., and Greenberg, M.E. (2006). Activity-dependent regulation of MEF2 transcription factors suppresses excitatory synapse number. Science *311*, 1008–1012.

15. Li, Z., McKercher, S.R., Cui, J., Nie, Z., Soussou, W., Roberts, A.J., Sallmen, T., Lipton, J.H., Talantova, M., Okamoto, S.-I., and Lipton, S.A. (2008). Myocyte enhancer factor 2C as a neurogenic and antiapoptotic transcription factor in murine embryonic stem cells. J. Neurosci. *28*, 6557–6568.

16. Barbosa, A.C., Kim, M.-S., Ertunc, M., Adachi, M., Nelson, E.D., McAnally, J., Richardson, J.A., Kavalali, E.T., Monteggia, L.M., Bassel-Duby, R., and Olson, E.N. (2008). MEF2C, a transcription factor that facilitates learning and memory by negative regulation of synapse numbers and function. Proc. Natl. Acad. Sci. USA *105*, 9391–9396.

17. Harrington, A.J., Bridges, C.M., Berto, S., Blankenship, K., Cho, J.Y., Assali, A., Siemsen, B.M., Moore, H.W., Tsvetkov, E., Thielking, A., et al. (2020). MEF2C hypofunction in neuronal and neuroimmune populations produces MEF2C haploinsufficiency syndrome–like behaviors in mice. Biol. Psychiatry *88*, 488–499.

18. Neale, B.M., Kou, Y., Liu, L., Ma'ayan, A., Samocha, K.E., Sabo, A., Lin, C.-F., Stevens, C., Wang, L.-S., Makarov, V., et al. (2012). Patterns and rates of exonic de novo mutations in autism spectrum disorders. Nature *485*, 242–245.

19. Hamdan, F.F., Myers, C.T., Cossette, P., Lemay, P., Spiegelman, D., Laporte, A.D., Nassif, C., Diallo, O., Monlong, J., Cadieux-Dion, M., et al. (2017). High rate of recurrent de novo mutations in developmental and epileptic encephalopathies. Am. J. Hum. Genet. *101*, 664–685.

20. Coe, B.P., Witherspoon, K., Rosenfeld, J.A., van Bon, B.W.M., Vulto-van Silfhout, A.T., Bosco, P., Friend, K.L., Baker, C., Buono, S., Vissers, L.E.L.M., et al. (2014). Refining analyses of copy number variation identifies specific genes associated with developmental delay. Nat. Genet. *46*, 1063–1071.

21. Deciphering Developmental Disorders Study (2015). Large-scale discovery of novel genetic causes of developmental disorders. Nature *519*, 223–228.

22. Fu, J.M., Satterstrom, F.K., Peng, M., Brand, H., Collins, R.L., Dong, S., Wamsley, B., Klei, L., Wang, L., Hao, S.P., et al. (2022). Rare coding variation provides insight into the genetic architecture and phenotypic context of autism. Nat. Genet. *54*, 1320–1331.

23. Werling, D.M., Brand, H., An, J.-Y., Stone, M.R., Zhu, L., Glessner, J.T., Collins, R.L., Dong, S., Layer, R.M., Markenscoff-Papadimitriou, E., et al. (2018). An analytical framework for whole-genome sequence association studies and its implications for autism spectrum disorder. Nat. Genet. *50*, 727–736.

24. An, J.-Y., Lin, K., Zhu, L., Werling, D.M., Dong, S., Brand, H., Wang, H.Z., Zhao, X., Schwartz, G.B., Collins, R.L., et al. (2018). Genome-wide de novo risk score implicates promoter variation in autism spectrum disorder. Science *362*, eaat6576.

25. Aneichyk, T., Hendriks, W.T., Yadav, R., Shin, D., Gao, D., Vaine, C.A., Collins, R.L., Domingo, A., Currall, B., Stortchevoi, A., et al. (2018). Dissecting the causal mechanism of X-linked dystonia-parkinsonism by integrating genome and transcriptome assembly. Cell *172*, 897–909.e21.

26. Padhi, E.M., Hayeck, T.J., Cheng, Z., Chatterjee, S., Mannion, B.J., Byrska-Bishop, M., Willems, M., Pinson, L., Redon, S., Benech, C., et al. (2021). Coding and noncoding variants in EBF3 are involved in HADDS and simplex autism. Hum. Genomics *15*, 44.

27. Oz-Levi, D., Olender, T., Bar-Joseph, I., Zhu, Y., Marek-Yagel, D., Barozzi, I., Osterwalder, M., Alkelai, A., Ruzzo, E.K., Han, Y., et al. (2019). Noncoding deletions reveal a gene that is critical for intestinal function. Nature *571*, 107–111.

28. Lieberman-Aiden, E., van Berkum, N.L., Williams, L., Imakaev, M., Ragoczy, T., Telling, A., Amit, I., Lajoie, B.R., Sabo, P.J., Dorschner, M.O., et al. (2009). Comprehensive mapping of long-range interactions reveals folding principles of the human genome. Science *326*, 289–293.

29. Schwarzer, W., Abdennur, N., Goloborodko, A., Pekowska, A., Fudenberg, G., Loe-Mie, Y., Fonseca, N.A., Huber, W., Haering, C.H., Mirny, L., and Spitz, F. (2017). Two independent modes of chromatin organization revealed by cohesin removal. Nature *551*, 51–56.

30. Ruiz-Velasco, M., Kumar, M., Lai, M.C., Bhat, P., Solis-Pinson, A.B., Reyes, A., Kleinsorg, S., Noh, K.-M., Gibson, T.J., and Zaugg, J.B. (2017). CTCF-mediated chromatin loops between promoter and gene body regulate alternative splicing across individuals. Cell Syst. *5*, 628–637.e6.

31. Rao, S.S.P., Huntley, M.H., Durand, N.C., Stamenova, E.K., Bochkov, I.D., Robinson, J.T., Sanborn, A.L., Machol, I., Omer, A.D., Lander, E.S., and Aiden, E.L. (2014). A 3D map of the human genome at kilobase resolution reveals principles of chromatin looping. Cell *159*, 1665–1680.

32. Rao, S.S.P., Huang, S.-C., Glenn St Hilaire, B., Engreitz, J.M., Perez, E.M., Kieffer-Kwon, K.-R., Sanborn, A.L., Johnstone, S.E., Bascom, G.D., Bochkov, I.D., et al. (2017). Cohesin loss eliminates all loop domains. Cell *171*, 305–320.e24.

33. Franke, M., Ibrahim, D.M., Andrey, G., Schwarzer, W., Heinrich, V., Schöpflin, R., Kraft, K., Kempfer, R., Jerković, I., Chan, W.-L., et al. (2016). Formation of new chromatin

---

domains determines pathogenicity of genomic duplications. Nature *538*, 265–269.

34. Lupiáñez, D.G., Kraft, K., Heinrich, V., Krawitz, P., Brancati, F., Klopocki, E., Horn, D., Kayserili, H., Opitz, J.M., Laxova, R., et al. (2015). Disruptions of topological chromatin domains cause pathogenic rewiring of gene-enhancer interactions. Cell *161*, 1012–1025.

35. Laugsch, M., Bartusel, M., Rehimi, R., Alirzayeva, H., Karaolidou, A., Crispatzu, G., Zentis, P., Nikolic, M., Bleckwehl, T., Kolovos, P., et al. (2019). Modeling the pathological long-range regulatory effects of human structural variation with patient-specific hiPSCs. Cell Stem Cell *24*, 736–752.e12.

36. Ghavi-Helm, Y., Jankowski, A., Meiers, S., Viales, R.R., Korbel, J.O., and Furlong, E.E.M. (2019). Highly rearranged chromosomes reveal uncoupling between genome topology and gene expression. Nat. Genet. *51*, 1272–1282.

37. Despang, A., Schöpflin, R., Franke, M., Ali, S., and Jerković, I. (2019). Functional dissection of the Sox9–Kcnj2 locus identifies nonessential and instructive roles of TAD architecture. Nature.

38. Redin, C., Brand, H., Collins, R.L., Kammin, T., Mitchell, E., Hodge, J.C., Hanscom, C., Pillalamarri, V., Seabra, C.M., Abbott, M.-A., et al. (2017). The genomic landscape of balanced cytogenetic abnormalities associated with human congenital anomalies. Nat. Genet. *49*, 36–45.

39. Firth, H.V., Richards, S.M., Bevan, aP., Clayton, S., Corpas, M., Rajan, D., Van Vooren, S., Moreau, Y., Pettett, R.M., and Carter, N.P. (2009). Decipher: database of chromosomal imbalance and phenotype in humans using ensembl resources. Am. J. Hum. Genet. *84*, 524–533.

40. Hsu, P.D., Scott, D.A., Weinstein, J.A., Ran, F.A., Konermann, S., Agarwala, V., Li, Y., Fine, E.J., Wu, X., Shalem, O., et al. (2013). DNA targeting specificity of RNA-guided Cas9 nucleases. Nat. Biotechnol. *31*, 827–832.

41. Pliatsika, V., and Rigoutsos, I. (2015). Off-Spotter": very fast and exhaustive enumeration of genomic lookalikes for designing CRISPR/Cas guide RNAs. Biol. Direct *10*, 4.

42. Zhang, Y., Pak, C., Han, Y., Ahlenius, H., Zhang, Z., Chanda, S., Marro, S., Patzke, C., Acuna, C., Covy, J., et al. (2013). Rapid single-step induction of functional neurons from human pluripotent stem cells. Neuron *78*, 785–798.

43. Dobin, A., Davis, C.A., Schlesinger, F., Drenkow, J., Zaleski, C., Jha, S., Batut, P., Chaisson, M., and Gingeras, T.R. (2013). STAR: ultrafast universal RNA-seq aligner. Bioinformatics *29*, 15–21.

44. DeLuca, D.S., Levin, J.Z., Sivachenko, A., Fennell, T., Nazaire, M.-D., Williams, C., Reich, M., Winckler, W., and Getz, G. (2012). RNA-SeQC: RNA-seq metrics for quality control and process optimization. Bioinformatics *28*, 1530–1532.

45. Love, M.I., Huber, W., and Anders, S. (2014). Moderated estimation of fold change and dispersion for RNA-seq data with DESeq2. Genome Biol. *15*, 550.

46. Leek, J.T. (2014). svaseq: removing batch effects and other unwanted noise from sequencing data. Nucleic Acids Res. *42*, e161.

47. Langfelder, P., and Horvath, S. (2008). WGCNA: an R package for weighted correlation network analysis. BMC Bioinf. *9*, 559.

48. Liberzon, A., Subramanian, A., Pinchback, R., Thorvaldsdóttir, H., Tamayo, P., and Mesirov, J.P. (2011). Molecular signatures database (MSigDB) 3.0. Bioinformatics *27*, 1739–1740.

49. Liberzon, A., Birger, C., Thorvaldsdóttir, H., Ghandi, M., Mesirov, J.P., and Tamayo, P. (2015). The molecular signatures database (MSigDB) hallmark gene set collection. Cell Syst. *1*, 417–425.

50. Harrington, A.J., Raissi, A., Rajkovich, K., Berto, S., Kumar, J., Molinaro, G., Raduazzo, J., Guo, Y., Loerwald, K., Konopka, G., et al. (2016). MEF2C regulates cortical inhibitory and excitatory synapses and behaviors relevant to neurodevelopmental disorders. Elife *5*, e20059.

51. Koopmans, F., van Nierop, P., Andres-Alonso, M., Byrnes, A., Cijsouw, T., Coba, M.P., Cornelisse, L.N., Farrell, R.J., Goldschmidt, H.L., Howrigan, D.P., et al. (2019). SynGO: an evidence-based, expert-curated knowledge base for the synapse. Neuron *103*, 217–234.e4.

52. ENCODE Project Consortium (2012). An integrated encyclopedia of DNA elements in the human genome. Nature *489*, 57–74.

53. Parikshak, N.N., Luo, R., Zhang, A., Won, H., Lowe, J.K., Chandran, V., Horvath, S., and Geschwind, D.H. (2013). Integrative functional genomic analyses implicate specific molecular pathways and circuits in autism. Cell *155*, 1008–1021.

54. Li, M., Santpere, G., Imamura Kawasawa, Y., Evgrafov, O.V., Gulden, F.O., Pochareddy, S., Sunkin, S.M., Li, Z., Shin, Y., Zhu, Y., et al. (2018). Integrative functional genomic analysis of human brain development and neuropsychiatric risks. Science *362*, eaat7615.

55. Doncheva, N.T., Morris, J.H., Gorodkin, J., and Jensen, L.J. (2019). Cytoscape stringapp: network analysis and visualization of proteomics data. J. Proteome Res. *18*, 623–632.

56. Buenrostro, J.D., Wu, B., Chang, H.Y., and Greenleaf, W.J. (2015). ATAC-seq: A method for assaying chromatin accessibility genome-wide. Curr. Protoc. Mol. Biol. *109*, 21–29.

57. Langmead, B., and Salzberg, S.L. (2012). Fast gapped-read alignment with Bowtie 2. Nat. Methods *9*, 357–359.

58. Zhang, Y., Liu, T., Meyer, C.A., Eeckhoute, J., Johnson, D.S., Bernstein, B.E., Nusbaum, C., Myers, R.M., Brown, M., Li, W., and Liu, X.S. (2008). Model-based analysis of ChIP-Seq (MACS). Genome Biol. *9*, R137.

59. Li, Q., Brown, J.B., Huang, H., and Bickel, P.J. (2011). Measuring reproducibility of high-throughput experiments. Ann. Appl. Stat. *5*, 1752–1779.

60. Hinrichs, A.S., Karolchik, D., Baertsch, R., Barber, G.P., Bejerano, G., Clawson, H., Diekhans, M., Furey, T.S., Harte, R.A., Hsu, F., et al. (2006). The UCSC /Genome browser database: update 2006. Nucleic Acids Res. *34*, D590–D598.

61. Schwartzman, O., Mukamel, Z., Oded-Elkayam, N., Olivares-Chauvet, P., Lubling, Y., Landan, G., Izraeli, S., and Tanay, A. (2016). UMI-4C for quantitative and targeted chromosomal contact profiling. Nat. Methods *13*, 685–691.

62. Ramos-Rodríguez, M., Subirana-Granés, M., and Pasquali, L. (2021). UMI4Cats: an R package to analyze chromatin contact profiles obtained by UMI-4C. Bioinformatics.

63. Subramanian, A., Tamayo, P., Mootha, V.K., Mukherjee, S., Ebert, B.L., Gillette, M.A., Paulovich, A., Pomeroy, S.L., Golub, T.R., Lander, E.S., and Mesirov, J.P. (2005). Gene set enrichment analysis: a knowledge-based approach for interpreting genome-wide expression profiles. Proc. Natl. Acad. Sci. USA *102*, 15545–15550.

64. Karczewski, K.J., Francioli, L.C., Tiao, G., Cummings, B.B., Alföldi, J., Wang, Q., Collins, R.L., Laricchia, K.M., Ganna, A., Birnbaum, D.P., et al. (2020). The mutational constraint

spectrum quantified from variation in 141, 456 humans. Nature *581*, 434–443.

65. Byrne, K., Vuocolo, T., Gondro, C., White, J.D., Cockett, N.E., Hadfield, T., Bidwell, C.A., Waddell, J.N., and Tellam, R.L. (2010). A gene network switch enhances the oxidative capacity of ovine skeletal muscle during late fetal development. BMC Genom. *11*, 378.

66. Bartlett, T.E., Müller, S., and Diaz, A. (2017). Single-cell Co-expression subnetwork analysis. Sci. Rep. *7*, 15066.

67. Gómez-Ferrería, M.A., and Rey-Campos, J. (2003). Functional domains of FOXJ2. J. Mol. Biol. *329*, 631–644.

68. Abad, M., Hashimoto, H., Zhou, H., Morales, M.G., Chen, B., Bassel-Duby, R., and Olson, E.N. (2017). Notch inhibition enhances cardiac reprogramming by increasing MEF2C transcriptional activity. Stem Cell Rep. *8*, 548–560.

69. Vedantham, V., Evangelista, M., Huang, Y., and Srivastava, D. (2013). Spatiotemporal regulation of an Hcn4 enhancer defines a role for Mef2c and HDACs in cardiac electrical patterning. Dev. Biol. *373*, 149–162.

70. Materna, S.C., Sinha, T., Barnes, R.M., Lammerts van Bueren, K., and Black, B.L. (2019). Cardiovascular development and survival require Mef2c function in the myocardial but not the endothelial lineage. Dev. Biol. *445*, 170–177.

71. Mayers, C.M., Wadell, J., McLean, K., Venere, M., Malik, M., Shibata, T., Driggers, P.H., Kino, T., Guo, X.C., Koide, H., et al. (2010). The Rho guanine nucleotide exchange factor AKAP13 (BRX) is essential for cardiac development in mice. J. Biol. Chem. *285*, 12344–12354.

72. Wang, W., Org, T., Montel-Hagen, A., Pioli, P.D., Duan, D., Israely, E., Malkin, D., Su, T., Flach, J., Kurdistani, S.K., et al. (2016). MEF2C protects bone marrow B-lymphoid progenitors during stress haematopoiesis. Nat. Commun. *7*, 12376.

73. Wang, W., Montel-Hagen, A., Sasidharan, R., and Mikkola, H.K.A. (2012). Mef2c maintains B cell homeostasis through the regulation of DNA repair machinery. Blood *120*, 278.

74. Franceschini, A.; and Others (2013). STRINGdb package vignette. Nucleic Acids Res.

75. Szklarczyk, D., Morris, J.H., Cook, H., Kuhn, M., Wyder, S., Simonovic, M., Santos, A., Doncheva, N.T., Roth, A., Bork, P., et al. (2017). The STRING database in 2017: quality-controlled protein–protein association networks, made broadly accessible. Nucleic Acids Res. *45*, D362–D368.

76. Cline, M.S., Smoot, M., Cerami, E., Kuchinsky, A., Landys, N., Workman, C., Christmas, R., Avila-Campilo, I., Creech, M., Gross, B., et al. (2007). Integration of biological networks and gene expression data using Cytoscape. Nat. Protoc. *2*, 2366–2382.

77. Saito, R., Smoot, M.E., Ono, K., Ruscheinski, J., Wang, P.-L., Lotia, S., Pico, A.R., Bader, G.D., and Ideker, T. (2012). A travel guide to cytoscape plugins. Nat. Methods *9*, 1069–1076.

78. Shannon, P., Markiel, A., Ozier, O., Baliga, N.S., Wang, J.T., Ramage, D., Amin, N., Schwikowski, B., and Ideker, T. (2003). Cytoscape: a software environment for integrated models of biomolecular interaction networks. Genome Res. *13*, 2498–2504.

79. Lemke, J.R., Lal, D., Reinthaler, E.M., Steiner, I., Nothnagel, M., Alber, M., Geider, K., Laube, B., Schwake, M., Finsterwalder, K., et al. (2013). Mutations in GRIN2A cause idiopathic focal epilepsy with rolandic spikes. Nat. Genet. *45*, 1067–1072.

80. Shi, X., Yasumoto, S., Kurahashi, H., Nakagawa, E., Fukasawa, T., Uchiya, S., and Hirose, S. (2012). Clinical spectrum of SCN2A mutations. Brain Dev. *34*, 541–545.

81. Salpietro, V., Dixon, C.L., Guo, H., Bello, O.D., Vandrovcova, J., Efthymiou, S., Maroofian, R., Heimer, G., Burglen, L., Valence, S., et al. (2019). AMPA receptor GluA2 subunit defects are a cause of neurodevelopmental disorders. Nat. Commun. *10*, 3094.

82. Floris, C., Rassu, S., Boccone, L., Gasperini, D., Cao, A., and Crisponi, L. (2008). Two patients with balanced translocations and autistic disorder: CSMD3 as a candidate gene for autism found in their common 8q23 breakpoint area. Eur. J. Hum. Genet. *16*, 696–704.

83. Saitsu, H., Igarashi, N., Kato, M., Okada, I., Kosho, T., Shimokawa, O., Sasaki, Y., Nishiyama, K., Tsurusaki, Y., Doi, H., et al. (2011). De novo 5q14.3 translocation 121.5-kb upstream of MEF2C in a patient with severe intellectual disability and early-onset epileptic encephalopathy. Am. J. Med. Genet. *155A*, 2879–2884.

84. Shimojima, K., Okumura, A., Mori, H., Abe, S., Ikeno, M., Shimizu, T., and Yamamoto, T. (2012). De novo microdeletion of 5q14.3 excluding MEF2C in a patient with infantile spasms, microcephaly, and agenesis of the corpus callosum. Am. J. Med. Genet. *158A*, 2272–2276.

85. Yauy, K., Schneider, A., Ng, B.L., Gaillard, J.-B., Sati, S., Coubes, C., Wells, C., Tournaire, M., Guignard, T., Bouret, P., et al. (2019). Disruption of chromatin organisation causes MEF2C gene overexpression in intellectual disability: a case report. BMC Med. Genomics *12*, 116.

86. Schluth-Bolard, C., Diguet, F., Chatron, N., Rollat-Farnier, P.-A., Bardel, C., Afenjar, A., Amblard, F., Amiel, J., Blesson, S., Callier, P., et al. (2019). Whole genome paired-end sequencing elucidates functional and phenotypic consequences of balanced chromosomal rearrangement in patients with developmental disorders. J. Med. Genet. *56*, 526–535.

87. Vergult, S., Van Binsbergen, E., Sante, T., Nowak, S., Vanakker, O., Claes, K., Poppe, B., Van der Aa, N., van Roosmalen, M.J., Duran, K., et al. (2014). Mate pair sequencing for the detection of chromosomal aberrations in patients with intellectual disability and congenital malformations. Eur. J. Hum. Genet. *22*, 652–659.

88. D'haene, E., Bar-Yaacov, R., Bariah, I., Vantomme, L., Van Loo, S., Cobos, F.A., Verboom, K., Eshel, R., Alatawna, R., Menten, B., et al. (2020). A neuronal enhancer network upstream of MEF2C is compromised in patients with Rett like characteristics. Hum. Mol. Genet. *29*, 879–880.

89. Dixon, J.R., Selvaraj, S., Yue, F., Kim, A., Li, Y., Shen, Y., Hu, M., Liu, J.S., and Ren, B. (2012). Topological domains in mammalian genomes identified by analysis of chromatin interactions. Nature *485*, 376–380.

90. Porter, B., and Paciorkowski, A. (2015). MEF2C haploinsufficiency syndrome: A severe neurodevelopmental disorder with variable epilepsy. J. Pediatr. Epilepsy *01*, 171–178.

91. Paciorkowski, A.R., Traylor, R.N., Rosenfeld, J.A., Hoover, J.M., Harris, C.J., Winter, S., Lacassie, Y., Bialer, M., Lamb, A.N., Schultz, R.A., et al. (2013). MEF2C Haploinsufficiency features consistent hyperkinesis, variable epilepsy, and has a role in dorsal and ventral neuronal developmental pathways. Neurogenetics *14*, 99–111.

92. Borlot, F., Whitney, R., Cohn, R.D., and Weiss, S.K. (2019). MEF2C-related epilepsy: Delineating the phenotypic spectrum from a novel mutation and literature review. Seizure *67*, 86–90.

93. Rocha, H., Sampaio, M., Rocha, R., Fernandes, S., and Leão, M. (2016). MEF2C haploinsufficiency syndrome: Report of

a new MEF2C mutation and review. Eur. J. Med. Genet. *59*, 478–482.

94. Williamson, I., Kane, L., Devenney, P.S., Flyamer, I.M., Anderson, E., Kilanowski, F., Hill, R.E., Bickmore, W.A., and Lettice, L.A. (2019). Developmentally regulated Shh expression is robust to TAD perturbations. Development *146*, dev179523.

95. Reilly, S.K., Gosai, S.J., Gutierrez, A., Mackay-Smith, A., Ulirsch, J.C., Kanai, M., Mouri, K., Berenzy, D., Kales, S., Butler, G.M., et al. (2021). Direct characterization of cis-regulatory elements and functional dissection of complex genetic associations using HCR–FlowFISH. Nat. Genet. *53*, 1166–1176.

96. Palmer, E.E., Sachdev, R., Macintosh, R., Melo, U.S., Mundlos, S., Righetti, S., Kandula, T., Minoche, A.E., Puttick, C., Gayevskiy, V., et al. (2021). Diagnostic yield of whole genome sequencing after nondiagnostic exome sequencing or gene panel in developmental and epileptic encephalopathies. Neurology *96*, e1770–e1782.

97. Fudenberg, G., Kelley, D.R., and Pollard, K.S. (2020). Predicting 3D genome folding from DNA sequence with Akita. Nat. Methods *17*, 1111–1117.

98. Huynh, L., and Hormozdiari, F. (2019). TAD fusion score: discovery and ranking the contribution of deletions to genome structure. Genome Biol. *20*, 60.

99. Nieboer, M.M., and de Ridder, J. (2020). svMIL: predicting the pathogenic effect of TAD boundary-disrupting somatic structural variants through multiple instance learning. Bioinformatics *36*, i692–i699.